

# 1 Overview: Fusion of Radar Polarimetry and Numerical Atmospheric 2 Modelling Towards an Improved Understanding of Cloud and 3 Precipitation Processes

4 Silke Trömel<sup>1,2</sup>, Clemens Simmer<sup>1</sup>, Ulrich Blahak<sup>3</sup>, Armin Blanke<sup>1</sup>, Florian Ewald<sup>4</sup>, Michael Frech<sup>5</sup>,  
5 Mathias Gergely<sup>5</sup>, Martin Hagen<sup>4</sup>, Sabine Hörnig<sup>6</sup>, Tijana Janjic<sup>7</sup>, Heike Kalesse-[Los](#)<sup>6</sup>, Stefan Kneifel<sup>8</sup>,  
6 Christoph Knot<sup>7,9</sup>, Jana Mendrok<sup>3</sup>, Manuel Moser<sup>10,4</sup>, Gregor [Möller](#)<sup>7</sup>[Köcher](#)<sup>7</sup>, Kai Mühlbauer<sup>1</sup>,  
7 Alexander Myagkov<sup>11</sup>, Velibor Pejčic<sup>1</sup>, Patric Seifert<sup>12</sup>, Prabhakar Shrestha<sup>1</sup>, Audrey Teisseire<sup>12</sup>, Leonie  
8 von Terzi<sup>8</sup>, Eleni Tetoni<sup>4</sup>, Teresa Vogl<sup>6</sup>, Christiane Voigt<sup>10,4</sup>, Yuefei Zeng<sup>7</sup>, Tobias Zinner<sup>7</sup>, Johannes  
9 Quaas<sup>6</sup>

10 <sup>1</sup>Institute for Geosciences, Department of Meteorology, University of Bonn, Bonn, 53121, Germany

11 <sup>2</sup>Laboratory for Clouds and Precipitation Exploration, Geovorbund ABC/J, Bonn, 53121, Germany

12 <sup>3</sup>Deutscher Wetterdienst (DWD), Offenbach, 63067, Germany

13 <sup>4</sup>Institute for Physics of the Atmosphere, DLR, Oberpfaffenhofen, 82234, Germany

14 <sup>5</sup>Deutscher Wetterdienst (DWD), Observatorium Hohenpeißenberg, Hohenpeißenberg, 82383, Germany

15 <sup>6</sup>Institute for Meteorology, Universität Leipzig, Leipzig, 04103, Germany

16 <sup>7</sup>Meteorological Institute Munich, Ludwig-Maximilians-Universität München, 80333, Germany

17 <sup>8</sup>Institute of Geophysics and Meteorology, University of Cologne, 50969, Germany

18 <sup>9</sup>Faculty of Medicine, University of Augsburg, Augsburg, 86159 Germany

19 <sup>10</sup>Institute for Physics of the Atmosphere, University Mainz, Mainz, 55099, Germany

20 <sup>11</sup>Radiometer Physics GmbH, Meckenheim, 53340, Germany

21 <sup>12</sup>Leibniz Institute for Tropospheric Research (TROPOS), 04318 Leipzig, Germany

22  
23  
24 *Correspondence to:* Silke Trömel (silke.troemel@uni-bonn.de)

25 **Abstract.** Cloud and precipitation processes are still [at the](#) main source of uncertainties in numerical weather prediction and  
26 climate change projections. The Priority Program “Polarimetric Radar Observations meet Atmospheric Modelling (PROM)“,  
27 funded by the German Research Foundation (Deutsche Forschungsgemeinschaft, DFG), is guided by the hypothesis; that many  
28 uncertainties relate to the lack of observations suitable to challenge the representation of cloud and precipitation processes in  
29 atmospheric models. Such observations can, however, nowadays be provided e.g. by the recently installed dual-polarization  
30 C<sub>W</sub>-band weather radar network of the German national meteorological service in synergy with cloud radars and other  
31 instruments at German supersites and similar national networks increasingly available worldwide. While polarimetric radars  
32 potentially provide valuable in-cloud information e.g. on hydrometeor type, quantity, and microphysical cloud and  
33 precipitation processes, and atmospheric models employ increasingly [complex higher-moment](#) microphysical modules,

34 ~~considerable knowledge gaps still exist~~~~still considerable knowledge gaps exist~~ in the interpretation of the observations and  
35 ~~large uncertainties~~ in the optimal microphysics model process formulations. PROM is a coordinated interdisciplinary effort to  
36 intensify the use of polarimetric radar observations in data assimilation, which requires a thorough evaluation and improvement  
37 of parametrizations of moist processes in atmospheric models. As an overview article of the inter-journal special issue “Fusion  
38 of radar polarimetry and numerical atmospheric modelling towards an improved understanding of cloud and precipitation  
39 processes”, [this article](#) outlines the knowledge achieved in PROM during the past two years and gives perspectives for the  
40 next four years.

## 41 **1 Introduction and Objectives of the priority program**

42 ~~A~~The main source of uncertainty ~~in the models used in~~~~used for in~~ numerical weather prediction (NWP) and climate change  
43 projections are ~~the parametrizations of~~ cloud and precipitation processes ([Bauer et al., 2015](#)). A major part of these uncertainties  
44 can be attributed to missing observations suitable to challenge the representation of cloud and precipitation processes employed  
45 in atmospheric models. ~~Since several years a~~ wealth of new information on precipitation microphysics and generating  
46 processes can be gained from observations from polarimetric weather radars and their synergistic analysis at different  
47 frequencies. The dual-polarization upgrade of the United States National Weather Service (NWS) S-Band Weather  
48 Surveillance Radar 1988 Doppler (WSR-88D) network was completed in 2013. Germany finished upgrading its C-band  
49 network to polarimetry in 2015 in parallel ~~with~~ other European countries. [The synergistic exploitation of polarimetric  
50 precipitation radars](#) ~~Together with measurements from cloud radars and other instrumentation available at supersites and  
51 research institutions their synergetic exploitation~~ enables for the first time a thorough evaluation and potential improvement  
52 of current microphysical parameterizations based on detailed multi-frequency remote-sensing observations. Data assimilation  
53 merges observations and models for state estimation as a prerequisite for prediction and can be ~~seen~~~~considered~~ as a smart  
54 interpolation between observations while exploiting the physical consistency of atmospheric models as mathematical  
55 constraints.

56 Considerable knowledge gaps still exist, however, both in radar polarimetry and atmospheric models, which still impede the  
57 full exploitation of the triangle ~~between~~ radar polarimetry, ~~atmospheric models,~~ ~~and~~ data assimilation and called for a  
58 coordinated interdisciplinary effort. The German Research Foundation (Deutsche Forschungsgemeinschaft, DFG) responded  
59 to this call and established the Priority Program ~~“Polarimetric Radar Observations meet Atmospheric Modelling (PROM)”~~;  
60 its first 3-year funding period ~~began in~~~~started~~ 2019, which will be followed by a second funding period starting in 2022. PROM  
61 ~~will~~ exploits the synergy of polarimetric radar observations and state-of-the-art atmospheric models to better understand moist  
62 processes in the atmosphere, and to improve their representation in climate- and weather prediction models. The overarching  
63 goal is to extend our scientific understanding at the verges of the three disciplines, radar polarimetry – atmospheric models –

64 data assimilation, for better predictions of precipitating cloud systems. To approach this goal the initiators of PROM at the  
65 Universities of Bonn and Leipzig in Germany identified the following five objectives (see also Trömel et al. 2018):

66 1) Exploitation of radar polarimetry for quantitative process detection in precipitating clouds and for model evaluation  
67 [including e.g. a quantitative analysis of polarimetric fingerprints and microphysical retrievals](#).

68 2) Improvement of cloud and precipitation schemes in atmospheric models based on process fingerprints detectable in  
69 polarimetric observations,

70 3) Monitoring of the energy budget evolution due to phase changes in the cloudy, precipitating atmosphere for a better  
71 understanding of its dynamics,

72 4) ~~Analyzing~~ ~~Generation of~~ precipitation system ~~analyses~~ by assimilation of polarimetric radar observations into atmospheric  
73 models for weather forecasting, and

74 5) Radar-based detection of the initiation of convection for the improvement of thunderstorm prediction.

75 In the first funding period, 14 projects (see <https://www2.meteo.uni-bonn.de/spp2115>) distributed over Germany contribute to  
76 at least one of these objectives. In most projects, a radar meteorologist works together with a modeller in order to successfully  
77 combine expert knowledge from both research fields. This overview article of the ACP/AMT/GMD inter-journal special issue  
78 entitled “Fusion of radar polarimetry and numerical atmospheric modelling towards an improved understanding of cloud and  
79 precipitation processes” outlines methodologies developed and results achieved from a selection of the projects during the past  
80 two years, and provides overall perspectives for the next four years. The paper is organized as follows: Section 2 explains  
81 prevailing challenges in the representation of clouds in atmospheric models, while Sect. 3 provides methodologies to extend  
82 our insight in the microphysics of clouds and precipitation by exploiting radar polarimetry. Section 4 addresses the fusion of  
83 ~~both disciplines~~—numerical modelling and radar polarimetry—via model evaluation either in radar observation space using  
84 ~~observation forward~~ operators or using microphysical retrievals. First conclusions for improved model  
85 ~~parametrizations~~ ~~parameterizations~~ and for a better representation of model uncertainty in ~~the process of~~ radar data assimilation  
86 are drawn. Section 5 provides a summary and perspectives for the following years.

## 87 **2 Representation of clouds in atmospheric models**

88 The representation of cloud- and precipitation processes in atmospheric models is a central challenge for NWP and climate  
89 projections (e.g., [Boueher et al., 2013](#); Bauer et al., 2015; [Forster et al., 2021](#)), ~~which they~~ also impact offline hydrological  
90 models by ~~significantly~~ modulating the distribution of incoming solar radiation and precipitation and affecting the simulated  
91 hydrological processes such as evapotranspiration, runoff, and groundwater depths (e.g., Shrestha, 2021). While the primitive  
92 equations provide a solid theoretical basis for atmospheric model dynamics, the key diabatic processes that drive energetics  
93 and thus circulation, are ~~poorly~~ ~~hardly~~ resolved. ~~Important diabatic processes are linked. These are to~~ ~~the~~ cloud ~~and~~ precipitation  
94 microphysical ~~sal~~ ~~processes~~ acting at scales of micrometres and turbulent processes ranging from several to hundreds of meters.

95 While significant progress has been achieved by high-resolution modelling at the coarser end of this range (e.g., Heinze et al.,  
96 2017; Stevens et al., 2020), the intricate and complex microphysical processes ~~will~~ still require parameterizations in any  
97 dynamic atmospheric model down to [and including](#) the scale of direct numerical simulations (e.g., Mellado et al., 2009).

98 A key uncertainty in weather prediction and climate modelling results from the still ~~rudimentary~~ representation of moist  
99 processes and ~~from~~ the diabatic heating/cooling [the modelsthey](#) induce due to latent heat and their interaction with radiation.  
100 The generation and interpretation of past and future climate states [additionally has](#) ~~in addition~~ to consider changes in  
101 microphysical processes due to anthropogenic aerosol acting, e.g., as cloud condensation nuclei and ice nucleating particles.  
102 For short-term weather prediction, the location and evolution of convective events with lifetimes of hours or less are  
103 particularly challenging, while relatively slow moving and frontal systems with lifetimes of days show reasonable  
104 predictability (Alifieri et al., 2012). ~~High-resolution simulations and observations of fronts point at their composition of small-~~  
105 ~~scale filament type short-lived convective features, but their importance for the system evolution (and predictability) is not yet~~  
106 ~~fully understood.~~

107 Atmospheric modelling in Germany has recently seen substantial advances both in terms of cloud-resolving simulations in  
108 NWP mode and in the implementation of ice and mixed-phase precipitation formation processes. Traditionally, different model  
109 systems were used for NWP and climate modelling, which were also both heavily used in academic research. Research with  
110 the ECHAM ([the acronym is a combination of ECMWF \(European Centre for Medium-Range Weather Forecasts\) and](#)  
111 [Hamburg](#)) model family originating from the NWP model of the ~~European Centre for Medium-Range Weather Forecasts~~  
112 ~~(ECMWF)~~ focused on long-term climate integrations at horizontal resolutions ~~onf~~ the order of 100 km (Stevens et al., 2013),  
113 and the COSMO model operated at horizontal resolutions down to 2.8 km was used for NWP and reanalysis studies. Both  
114 model families are currently [being](#) replaced by the ICOSahedral Nonhydrostatic (ICON) modelling framework (Zängl et al.,  
115 2015) jointly developed by [the](#) Max-Planck Institute for Meteorology and the German national meteorological service  
116 (Deutscher Wetterdienst, DWD). Its climate version (the ICON general circulation model, ICON GCM) inherited its physics  
117 package from the ECHAM model, and the NWP version incorporated the one from the COSMO model. A third version largely  
118 based on the COSMO physics package was developed for higher resolutions (Dipankar et al., 2015) and employs a large-eddy  
119 turbulence scheme (ICON-LEM). The latter is able to operate on large domains (Heinze et al., 2017; Stevens et al., 2020) and  
120 includes aerosol-cloud interactions (Costa-Surós et al., 2020). In PROM, primarily ~~the three~~ [the three ICON model variants](#)  
121 ~~is variants are used, in its three different variants (ICON-LEM, ICON-NWP, and ICON-A/GCM) are used.~~

122 In most atmospheric models, cloud and precipitation microphysical processes are represented by bulk microphysical schemes  
123 that distinguish between different hydrometeor classes and include their specific masses as prognostic variables while their  
124 size distributions are parameterized ([the ICON model considered here uses the scheme by Seifert and Beheng, 2006](#)).  
125 Computationally much more demanding are so-called spectral-bin microphysics schemes (Khain et al., 2015), which evolve  
126 cloud- and precipitation particle size distributions discretized into size-interval bins. An example is the Hebrew University

127 ~~C~~cloud ~~M~~odel (HUCM) created by Khain et al. (2005) that treats both liquid and much more intricate (~~since ice may occur~~  
128 ~~in various shapes and densities~~) ice crystal distributions. The model is employed by some of the PROM projects in addition to  
129 the liquid-only bin-microphysics model by Simmel et al. (2015) extended ~~to~~ the ice phase based on the scheme by Hashino  
130 and Tripoli (2007). For the simulation of the evolution of specific air volumes a Lagrangian particle model (McSnow; Brdar  
131 and Seifert, 2018) is used in PROM, that models ice and mixed-phase microphysical processes such as depositional growth,  
132 aggregation, riming, secondary ice generation, and melting closer to the real processes than bulk formulations. Microphysical  
133 processes including radiation-particle interactions obviously depend on particle shape; thus the evolution of shapes in particle  
134 models – and their signatures in radar observations – is instrumental for a full understanding and adequate representation of  
135 the microphysical processes in models. Advanced microphysical ~~parametrizations~~parameterizations such as spectral-bin or  
136 Lagrangian particle schemes are relevant for cloud-resolving models and exploited ~~in PROM~~ for the development and  
137 improvement of bulk parametrizations. Scientific questions about global climate ~~require~~ecessitate long model integrations  
138 and thus coarse spatial resolutions ~~due to computing time constraints. At these~~oarse resolutions (usually of order of 100 x 100  
139 ~~km<sup>2</sup> in the horizontal~~), it is insufficient to allow cloud formation only for grid boxes that reach relative humidity of 100%.  
140 ~~Rather, fractional cloudiness needs to be considered when , i.e. the occurrence of clouds even if the grid-box mean relative~~  
141 ~~humidity is below 100%, which~~–This ~~requires~~implies the ~~which~~ requirement of parametrizations of subgrid-scale variability  
142 ~~in relative humidity, and with this, of the spatial cloud variability.~~ Here, PROM builds on assumptions employed in the  
143 global ICON model (ICON GCM) to predict fractional cloudiness (e.g., Quaas, 2012).

### 144 3 Observational insights from polarimetric radar observations and ~~remaining~~ challenges

145 DWD operates 17 state-of-the-art polarimetric Doppler C-band weather radars which provide a 3-D sampling of  
146 precipitating ~~on~~ particles ~~in the lower atmosphere above Germany~~processes every five minutes. Together with their ~~ir~~ Doppler  
147 information ~~from those systems~~, radars ~~are~~–data–are the backbone for precipitation and nowcasting products for all  
148 meteorological services. Although precipitation monitoring is still the most widespread application of weather radars, their  
149 upgrade to polarimetry worldwide not only ~~improves~~improve precipitation estimates; ~~but~~–their observations are also  
150 increasingly exploited for the evaluation and improvement of the representation of cloud- and precipitation processes in  
151 atmospheric models (e.g., Gao et al., 2011; Jung et al., 2012; You et al., 2020; Wang et al., 2020). Additional observations  
152 from cloud radars nowadays available at so-called supersites (in Germany e.g., the Jülich Observatory for Cloud Evolution –  
153 Core Facility; JOYCE-~~CFef~~; Löhnert et al. 2015; http://www.cpep-lab.de), universities, and research facilities (e.g. the Leipzig  
154 Aerosol and Cloud Remote Observations System; LACROS; Bühl et al., 2013) open ~~additional~~ opportunities to inform and  
155 improve atmospheric models. The use of shorter wavelengths of cloud radars shifts the sensitivity of the observations towards  
156 smaller particles and partly increases the ~~magnitudes~~strength of the received polarimetric signals (e.g.  $K_{DP}$  – the ~~differential~~  
157 phase ~~shift~~change between horizontal and vertical polarization per distance called specific differential ~~phase~~change – scales  
158 with  $\lambda^{-1}$ ), which allows for more detailed studies of ice and cloud microphysics. Polarimetric and multi-frequency radar

159 observations ~~allow for a more granular look at~~ ~~allow even more to zoom in~~ microphysical processes and provide a great data  
160 base for model evaluation, the improvement of microphysical ~~parameterizations~~ ~~parameterizations~~, and data assimilation, and  
161 thus have the potential to significantly improve both weather forecasts and climate predictions.

### 162 3.1 Multi-frequency and spectral polarimetry for ice and cloud microphysics

163 The PROM-project *Understanding Ice Microphysical Processes by combining multi-frequency and spectral Radar*  
164 *polarimetry and super-particle modelling (IMPRINT)* ~~aims to improve~~ ~~at improving~~ ice microphysical process  
165 understanding by using ~~spectral~~ multi-frequency and ~~spectral~~ radar polarimetric observations in combination with Monte-Carlo  
166 Lagrangian super-particle modeling (Brdar and Seifert, 2018). ~~The main focus of our analysis are~~ ~~M~~mid-latitude stratiform  
167 clouds, ~~which as they~~ occur frequently during winter time over JOYCE-CF, ~~are the main focus of~~ Radar polarimetric variables  
168 are well known to be particularly sensitive to the presence of asymmetric ice particles (e.g. Kumjian 2013). Only recently, also  
169 polarimetric cloud radars operating at Ka or W-band are ~~routinely~~ available ~~and routinely operated~~ (Oue et al. 2018; Myagkov  
170 et al. 2016; Bühl et al. 2016; Matrosov et al. 2012). Some polarimetric variables, ~~such as~~  $K_{DP}$ , are wavelength dependent ( $K_{DP}$   
171 is inversely proportional to the wavelength), which provides enhanced sensitivity to ice particle concentration at higher  
172 frequencies. Multi-frequency approaches are ~~very~~ complementary to radar polarimetry as they are sensitive to larger ice  
173 particles. Most commonly, the dual wavelength ratio (DWR), defined as the logarithmic difference of the effective reflectivity  
174  $Z_e$  at two frequencies, is used. ~~When the~~ ice particles ~~reaches a sizes where they~~ transition ~~ns~~ at the higher frequency from  
175 Rayleigh into non-Rayleigh scattering ~~from one wavelength to a higher one~~, the DWR increases, ~~which allows~~ ~~Hence, the~~  
176 ~~DWR is commonly used~~ to infer the characteristic size of the underlying size distribution. The ~~use of combination of three~~  
177 radar frequencies (e.g. X, Ka, W) extends the ~~discernable~~ size range, ~~which can be quantified with this method e.g. because for~~  
178 ~~example~~ e.g. the DWR of the Ka-W combination saturates for very large particles (Kneifel et al. 2015; Ori et al. 2021). The  
179 information content ~~of combined polarimetric and multi-frequency observations~~ can be further extended ~~if when not only~~  
180 ~~common radar moments but~~ also the full Doppler spectral information is explored. ~~The different fall velocities allow for~~ ~~t~~he  
181 separation of different hydrometeors; ~~due to their different fall velocities allows for example to separate~~ the high  $Z_{DR}$  signal  
182 originating from small, slow ~~falling~~ ice crystals ~~can be distinguished~~ from the also low  $Z_{DR}$  signal of ~~the~~ faster falling snow  
183 aggregates, which usually dominate the total  $Z_{DR}$ . Only ~~very~~ few studies used ~~so far~~ spectral polarimetric observations for ice  
184 and snow microphysical studies (Luke et al., 2021; Oue et al., 2018; Pfitzenmayer et al., 2018; Spek et al., 2008). The ~~new~~  
185 observations collected during the first multi-months winter campaign carried out at JOYCE-CF as part of the IMPRINT project  
186 ~~provide to the authors knowledge~~ for the first time the opportunity to investigate both, polarimetry and multi-frequency  
187 observations in the Doppler spectra space. Spectral polarimetry allows in particular to exploit the different terminal velocities  
188 of hydrometeor types to quantify their contributions to the total measured polarimetric quantity; e.g. the strong polarimetric  
189 signals generated by small ice particles can be separated from the weak polarimetric contribution of large aggregates to the  
190 total measured differential reflectivity in logarithmic scale  $Z_{DR}$ . The combination of spectral polarimetry with multi-  
191 frequency radar observations allows for the investigation of the evolution of particle sizes in detail. The dual wavelength ratio

(DWR), defined as the logarithmic difference of the effective reflectivity  $Z_e$  at two frequencies, allows to infer the mean size of the underlying particle size distribution. The scattering properties of the largest particles first transition at the higher frequency from the Rayleigh into the non-Rayleigh scattering regime causing the DWR to increase (Kneifel et al., 2015). In order to characterize a wide range of particle sizes, a combination of more than two radar frequencies has been found to be advantageous (e.g. Ori et al., 2020). An example is the analysis of of this extended view on ice microphysical processes in the dendritic growth layer DGL is illustrated in Fig. 1 for a snowfall event observed on 22nd January 2019 at JOYCE-CF. Especially in the upper half of the cloud, the  $Z_{DR}$  is enhanced while  $K_{DP}$  values are still low (Fig. 1b-c). Starting at the  $-15^\circ\text{C}$  isotherm, the  $Z_{DR}$  sharply decreases and shows an anti-correlation to the enhanced DWR (Fig. 1a) and  $K_{DP}$  values. These polarimetric signatures at  $-15^\circ\text{C}$  have been reported by numerous previous studies (e.g., Moisseev et al., 2015 among others), and also the DWR increase of DWR below the  $-15^\circ\text{C}$  level resembles very consistent to the examples shown in Oue et al. (2018). Oue et al 2018 concluded in agreement with findings in Moisseev et al. (2015), that an increasing concentration of asymmetric aggregates are partly responsible for the enhanced values of  $K_{DP}$  because the number of as the concentration of small ice particles will decrease is expected to be drastically reduced due to aggregation. The spectrally-resolved  $Z_{DR}$  ( $sZ_{DR}$ , Fig. 1e), however, reveals that high  $Z_{DR}$ -producing, slowly falling ice particles are still present down to the  $-5^\circ\text{C}$  level. The spectrally resolved DWR (Fig. 1d) shows that the particles falling from above into the DGL are already partly aggregated. At  $-17^\circ\text{C}$ , the spectra are much rapidly widened and a new spectral mode appears which is linked to the rapid  $sZ_{DR}$  increase found at that level (Fig. 1e). The new ice particle mode increases in Doppler velocity and sDWR until of up to 20dB are reached. Unlike  $Z_{DR}$ , the  $K_{DP}$  (Fig. Fig. 1c and f) remains enhanced at values between  $1-2^\circ/\text{km}$  down to the temperature level of  $-5^\circ\text{C}$  level. A possible explanation of the bimodal spectra - increased  $sZ_{DR}$  and  $K_{DP}$  - might be secondary ice processes such as collisional fragmentation (Field et al., 2017). The few existing laboratory studies indicated that the number of fragments ejected starts to rapidly increases at  $-20^\circ\text{C}$ , reaching a maximum at  $-17^\circ\text{C}$  and decreasing again towards  $-10^\circ\text{C}$  (Takahashi et al., 1995; Takahashi, 2014). This temperature dependence fits surprisingly well to the observed overall radar signatures observed in the DGL, although the laboratory studies only considered collisions of solid ice spheres. As we can exclude strongly rimed particles in our case study the snowfall case shown in Fig. 1, we speculate that fragile dendritic structures growing on the surface of aggregates might be responsible, which also grow on the surface of aggregates, which precipitates sediment into the DGL from above and might easily break into smaller pieces during particle collisions (Fig. 1d). Fig. 1a shows the DWR during snowfall at the ground observed at Ka and W band for 22nd January 2019 01-22 at over the "Jülich Observatory for Cloud Evolution - Core Facility" (JOYCE CFcf). At about 15 UTC, the DWR KaW strongly increases at in about 2300 m height indicating the onset of strong aggregation. While DWR is sensitive to large aggregates, high  $Z_{DR}$  (the difference between horizontal and vertical radar reflectivity,  $Z_H - Z_V$ ) indicates asymmetric particles (in the case of frozen precipitation it signals small ice crystals). Since  $Z_{DR}$  is an integral signal of the present particle size distribution (PSD), it is dominated by the larger aggregates and thus decreases at the height level where DWR KaW starts to rise (Fig. 1b).  $K_{DP}$  also starts to increase at this level (Fig. 1e), which may indicate secondary ice production. The spectrally resolved DWR KaW and  $Z_{DR}$  ( $sZ_{DR}$ ) at 15 UTC are shown in Figs 1d-e for more detailed insights. Enhanced DWR KaW on the left side of the spectrum indicates aggregates

Formatiert: Tiefgestellt

226 already present at temperatures colder than above  $-15^{\circ}\text{C}$  reaching maximum sizes at around  $-10^{\circ}\text{C}$ . The width of the DWR-  
227  $K_{aW}$  spectrum starts to increase rapidly already at around  $-17^{\circ}\text{C}$  resulting in a secondary spectral mode at  $-15^{\circ}\text{C}$ , and  $sZ_{DR}$   
228 reaches values of up to 3 dB for the slow falling particles. A possible interpretation of the bimodal DWR spectrum at increased  
229  $sZ_{DR}$  and  $K_{DR}$  is the fragmentation of delicate ice crystal structures, which have been found in laboratory studies to evolve  
230 close to  $-17^{\circ}\text{C}$  (Takahashi et al., 1995; Takahashi 2014). The fragmentation signal might not only relate to single crystals but  
231 could also be caused by dendritic structures growing at the surface of aggregates similar to the growth structures found on ice  
232 spheres at similar temperatures in the laboratory study by Takahashi (1993). ~~A central counterpart of the observations in~~  
233 ~~IMPRINT, are simulations with a Monte-Carlo Lagrangian super-particle model (Brdar and Seifert, 2018) simulations were~~  
234 ~~recently extended in IMPRINT by a habit prediction scheme and as well as a parameterization of ice collisional fragmentation~~  
235 ~~following provided by Phillips et al. (2017). Together with a radar forward operator, we are now able to study t~~  
236 ~~he role of ice fragmentation and other ice microphysical processes is currently investigated with a radar observation operator for explaining~~  
237 ~~the observed radar signatures of related to intense aggregation as shown in Fig. 1.~~

238  
239 The PROM-project *Investigation of the initiation of convection and the evolution of precipitation using simulations and*  
240 *polarimetric radar observations at C- and Ka-band (IcePolCKa)* combines ~~the~~ observations of the C-band Polarization  
241 Diversity Doppler Radar (POLDIRAD) at the German Aerospace Center (DLR), Oberpfaffenhofen, with those of the Ka-  
242 band, Millimeter-wave cloud Radar of the Munich Aerosol Cloud Scanner (miraMACS) at Ludwig-Maximilians-Universität  
243 (LMU), Munich. ~~While in contrast to IMPRINT aims at the combination of triple-frequency zenith-pointing observations~~  
244 ~~with spectral cloud radar polarimetry, the IcePolCKa project explores the life cycle of convective precipitation with the~~  
245 ~~feasibility of spatially separated weather and cloud radars to observe convective precipitation development along its life cycle~~  
246 ~~and more specifically in order to quantify narrow down ice crystal properties in precipitation formation. The project is focused in~~  
247 ~~a novel approach, to study the project is convective cells are studied with a focus on the ice particle growth and its role in~~  
248 ~~precipitation formation within convective cells.~~ Coordinated Range-Height-Indicator (RHI, varying elevation at constant  
249 azimuth) scans ~~along the 23 km long cross-section between both the two radar instruments, allow to track and observe provide~~  
250 ~~simultaneous measurements of the respective DWR (Fig. 2a) and  $Z_{DR}$  (Fig. 2b) fingerprints of individual convective cells,~~  
251 ~~along the 23 km long cross-section between the two radar instruments while convective cells are tracked. The While the~~  
252 ~~deviation from Rayleigh scattering with increasing ice crystal size at the cloud radar wavelength is used to distinguish regions~~  
253 ~~dominated by aggregation from regions with depositional growth, the slanted-wise perspective of the weather radar helps to~~  
254 ~~narrow down the aspect ratio of ice crystals. Although the DWR technique to infer ice crystal size is well-established (e.g.~~  
255 ~~Kneifel et al., 2015), it needs to make assumptions about the unknown ice crystal shape are necessary.~~ Here, simultaneous  
256 polarimetric measurements, like  $Z_{DR}$ , help to narrow down the average asphericity of ice crystals and reduce ambiguities in  
257 ~~retrieving ice crystal size and ice water content. In one part of IcePolCKa develops develops an algorithm is developed, which~~  
258 ~~use combines  $Z_H$ ,  $Z_{DR}$  and DWR measurements from the two spatially separated radars to retrieve IWC, the mean particle~~  
259 ~~diameter  $D_{eq}$ , and the aspect ratio of ice crystals. These parameters are retrieved iteratively based on using a least-squares fit~~

Formatiert: Tiefgestellt

Formatiert: Tiefgestellt

Formatiert: Tiefgestellt



260 between measurements and T-matrix scattering simulations. The model of horizontally aligned spheroids in combination with  
261 an effective medium approximation following Hogan et al (2012) is used to find the simplest ice particle model which is still  
262 able to explain the multi-wavelength polarimetric measurements; the model of horizontally aligned spheroids in combination  
263 with an effective medium approximation following Hogan et al (2012) is used. This approach allows one to study the  
264 covariance of DWR and  $Z_{DR}$  while seamlessly varying the particle density, the mean particle diameter  $D_m$ , and the aspect  
265 ratio. For this task, more sophisticated models, such as like DDA simulations of specific ice crystals, would require introducing  
266 additional challenges to define the knowledge of the aspect ratio, in the first place and make it hard to identify sort a collection  
267 of ice shape collections along these free variables. Parallel to the retrieval development, the multi-wavelength polarimetric  
268 we use our The polarimetric, multi-wavelength measurements are also used as a benchmark for convective precipitation  
269 formation in NWP models, where it is well known that cloud microphysics introduce substantial uncertainty to NWP  
270 simulations (e.g. Morrison et al., 2020, Xue et al., 2017). In IMPRINTA setup for systematic characterization of simulated  
271 microphysical processes in NWP models will be compared to in comparison to fingerprints in radar observations has been  
272 implemented: A nested WRF setup covering the overlap area of both radars is used to simulate convective events with  
273 microphysical schemes of varying complexity while the Cloud-resolving model Radar Simulator (CR-SIM; Oue et al.,  
274 2020), a development outside PROM, is applied to produce synthetic radar observations, such as like the DWR (Fig. 2c) and  
275  $Z_{DR}$  (Fig. 2d). Fig. 2 illustrates that the Predicted Particle Properties (P3) scheme (Morrison and Milbrandt, 2015) is able  
276 to produce DWR features of similar magnitude and variability compared to the observations, while a realistic ice particle  
277 asphericity is still missing. While previous studies only compared a limited number of microphysics schemes and days or were  
278 limited to case studies, the IcePolCKa project compiled over 30 convective days of polarimetric measurements and simulations  
279 with 5 different schemes over a 2-year period. IcePolCKa has collected a 2-year dataset, which is currently used to analyze  
280 the performance of different microphysical schemes on a sound statistical basis, which is. This dataset is currently used to  
281 analyze how well these different microphysical schemes can reproduce the polarimetric observations. To that end, a cell-  
282 tracking algorithm (TINT; Fridlind et al. 2019) facilitates the comparison on a cell object basis. For example, Fig. 2 illustrates  
283 that the Predicted Particle Properties (P3) scheme (Morrison and Milbrandt, 2015) is able to produce DWR features of  
284 similar magnitude and variability compared to the observations while a realistic ice particle asphericity is still missing.  
285 Comparison of macrophysical cloud characteristics, such as echo top height or maximum cell reflectivity, show that the model  
286 simulates too few weak and small scale convective cells, independent of the microphysics scheme. In ongoing studies, the P3  
287 scheme seems to better represent radar signatures within the ice phase, while a spectral bin scheme tends to better simulate  
288 radar signatures within rain, where all other schemes are not able to have issues in correctly reproducing observed  $Z_{DR}$  features.

289  
290 The PROM-project *A seamless column of the precipitation process from mixed-phase clouds employing data from a*  
291 *polarimetric C-band radar, a micro-rain radar and disdrometers (HydroColumn)* characterizes precipitation processes  
292 inside a vertical atmospheric column by combining polarimetric Doppler weather radar observations with co-located  
293 measurements from micro-rain radars, disdrometers and in-situ measurements, and by relating these high-resolution

Formatiert: Tiefgestellt

Formatiert: Tiefgestellt

294 observations to the large-scale atmospheric thermodynamics derived from NWP models. To date, spectral analyses are mostly  
295 performed with cloud radars operating at shorter wavelengths (see previous paragraphs [or, e.g., Shupe et al., 2004; Verlinde](#)  
296 [et al., 2013; Kalesse et al., 2016; Gehring et al., 2020; Li and Moisseev, 2020](#)), but their [implementation across the applicability](#)  
297 [to the national C-band radar network](#) offers prospects for operational area-wide applications, e.g.: the identification of dominant  
298 precipitation particle growth processes such as aggregation or riming. *HydroColumn* [uses the plans to provide the proof of](#)  
299 [concept that Doppler spectra measured at C-band during the operational DWD birdbath scan, that is used for monitoring the](#)  
300 [differential reflectivity \(Frech and Hubbert, 2020\), for the analysis of provide beneficial](#) microphysical process information.  
301 [As an example](#), Fig. 3 shows quasi-vertical profiles (QVPs; Trömel et al., 2014; Ryzhkov et al., 2016) of polarimetric variables  
302 and Doppler spectra from birdbath scans for a stratiform precipitation event monitored with the Hohenpeißenberg C-band  
303 research radar (47.8014N, 11.0097E) of DWD together with in-situ particle images obtained by the Falcon research aircraft  
304 from [the German Aerospace Center \(DLR\)](#) during the BLUESKY campaign (Voigt et al., 2021) within the *POLICE* project  
305 (Sect. [3.24.2.1](#)). In-situ measurements have been performed with the Cloud, Aerosol and Precipitation Probe CAPS (Kleine et  
306 al., 2018) integrated in a wing station on the Falcon flying within a horizontal distance of about 20 km from the radar site and  
307 within about  $\pm 15$  min of the radar measurements. [T Here, the dendritic growth layer \(DGL; Ryzhkov and Zrníc, 2019\)](#) centered  
308 around  $-15$  °C is characterized by  $Z_{DR}$  maxima of  $\sim 1$  dB and  $K_{DP}$  of  $\sim 0.2$  °  $\text{km}^{-1}$ , and a strong  $Z_H$ -increase towards lower  
309 levels (Fig. 3a). Particle images collected at temperatures [below about older than about](#)  $-15$  °C indicate mostly small irregular  
310 ice particles with the number of larger particles increasing toward  $-15$  °C (see levels L1 and L2 in Fig. 3c), and further down  
311 also reveal dendrites and plates (L3, L4). In general, aggregation and riming become highly effective particle growth  
312 mechanisms at temperatures around  $-7$  °C (Libbrecht, 2005), [and both processes](#) resulting in a reduction of  $Z_{DR}$  (Fig. 3a). [The](#)  
313 [y Here, vertically pointing Doppler measurements can be used here to gain a deeper insight into the particle growth process. In](#)  
314 [this specific case study, the absence of secondary spectral modes in the Doppler spectra at C-band combined with relatively](#)  
315 [slow mean Doppler velocities above the melting layer suggests aggregation instead of riming as the dominant growth process](#)  
316 [\(Fig. 3b\). the Doppler measurements illustrated in Fig. 3b indicate typical ice-particle fall speeds increasing to about  \$2 \text{ m s}^{-1}\$](#)   
317 [just above the melting layer and thus suggest a transition from predominantly aggregates to moderately rimed particles based](#)  
318 [on the relationship between Doppler velocity and riming degree found by Kneifel and Moisseev \(2020\). This conclusion is](#)  
319 [supported confirmed by the corresponding in-situ images showing irregular 3-D structures of occasionally very large size](#)  
320 [while no large supercooled liquid droplets required for significant riming were recorded \(L6\)-increasing riming of polycrystals](#)  
321 [and aggregates toward the melting layer \(L6\). The analysis confirms the benefit of interpreting radar signatures from](#)  
322 [polarimetric weather radar observations in combination with vertically pointing Doppler radar measurements toward a better](#)  
323 [understanding of precipitation microphysics, which was previously pointed out for higher-frequency cloud research radars](#)  
324 [\(Oue et al., 2018; Kumjian et al., 2020\). This novel application of radar spectral analysis to vertically-pointing operational](#)  
325 [weather radar scans may provide can also lead to a more detailed view into intense precipitation events, such as hailstorms,](#)  
326 [where the use of cloud radars is severely limited due to the strong attenuation at high radar frequencies.](#)

Formatiert: Hochgestellt

### 3.2. Anthropogenic modifications of precipitation microphysics

The PROM-project *Polarimetry Influenced by CCN and INP in Cyprus and Chile (PICNICC)* seeks to improve our understanding of aerosol effects on microphysical growth processes in mixed-phase clouds. *PICNICC* exploits unique remote-sensing datasets from the LACROS suite (Radenz et al., 2021) extended with ground-based remote sensing instruments installed at Leipzig University, Universidad de Magallanes (Punta Arenas), and Cyprus University of Technology (Limassol). Thus, dual-frequency polarimetric radar observations from the polluted, aerosol-burden Northern and from the clean, pristine Southern hemisphere can be contrasted for microphysical process studies as already performed in the project. For stratiform mixed-phase clouds and incorporating non-polarimetric cloud radar observations this was recently already successfully done to investigate inter-hemispheric contrasts in the efficiency of heterogeneous ice formation (Radenz et al., 2021). The *PICNICC* project challenges the hypothesis that since higher ice crystal concentrations favour aggregation, which the latter is expected to be more frequent for high aerosol loads and accordingly higher ice nucleating particle (INP) concentrations, while riming should prevail when supercooled liquid layers are sustained due to a scarcity of INP. Evaluating this hypothesis requires the distinction between aggregation and riming processes in mixed-phase cloud systems. Fig. 4 demonstrates for 30 August 2019, when a deep mixed-phase cloud system passed the low-aerosol site in Punta Arenas (53°S, 71°W), Chile, on 30 August 2019, the capability of the LACROS suite when combined with a 94-GHz Doppler radar at the low-aerosol site in Punta Arenas (53°S, 71°W), Chile, to distinguish between aggregates and rimed particles. The pattern of the 94-GHz radar reflectivity factor ( $Z$ , Fig. 4a) underlines the complex structure of the system. The height spectrogram of the vertical-pointing 94-GHz slanted linear depolarization ratio (SLDR, Fig. 4 e) from 08:30 UTC exhibits regions of changing shape signatures and multi-modality in the cloud radar Doppler spectra, where multiple hydrometeor populations coexist. The polarizability ratio  $\xi_e$  (Myagkov et al., 2016) (Fig. 4d) obtained from the RHI scans of SLDR and the co-cross correlation coefficient of horizontal and vertically polarized channels in the slanted basis  $\rho_{\theta}$  at 35-GHz (Fig. 4 b, c) the polarizability ratio  $\xi_e$  (Myagkov et al., 2016) is obtained (Fig. 4d), which allows us to estimate a density-weighted hydrometeor shape. For the purpose of shape classification, SLDR is more suited for shape classification compared to LDR. By slanting the polarization basis by 45°, the returned LDR signatures are much less sensitive to the canting angle distribution of the targets, especially at low elevation angles (Matrosov et al., 2001; Myagkov et al., 2016). The polarimetric RHI scans and the Doppler spectra data enable the retrieval of the vertical profile of the hydrometeors: Columnar-shaped bullet rosettes are formed between 2.5 km height and cloud top as indicated in the RHI scans by an elevation-constant SLDR (Fig. 4b) and an increase of  $\rho_{\theta}$  with decreasing elevation (Fig. 4c).  $\xi_e$  is around 1.3 (Fig. 4d), which is characteristic for slightly columnar crystals. Already at around 3 km height (-15 to -20°C) the decreasing elevation-dependence of  $\rho_{\theta}$ , already at around 3 km height (-15 to -20°C) suggests a more random particle orientations; here the W-band SLDR spectra (Fig. 4e) show reduced values, likely due to the co-existence of dendritic ice crystals, which are formed preferably in this temperature range and cause low SLDR at vertical stare. The co-location of dendrites and columnar crystals can be explained by either splintering of the arms of the dendritic crystals or a mixing of locally produced dendrites with columnar crystals from higher up, or both.

360 ~~At heights below 2.5 km,  $\xi$ , decreases toward unity, indicating the growth of isometric particles. Also the vertical-~~  
361 ~~pointing W-Band SLDR slowly decreases toward the cloud base, while fall velocities increase (Fig. 4e). Both features are~~  
362 ~~characteristic for riming, which is corroborated by co-located lidar observations that indicate detecting liquid water in the cloud-~~  
363 ~~base region (not shown). Availability of Doppler spectra profiles such as the one presented in Fig. 4e are also built used in the~~  
364 ~~basis for a new neural-network-based neural-network-based riming detection algorithm that was recently tailored by Vogl et~~  
365 ~~al. (2021) for vertical-pointing 94 GHz cloud radar observations. This Novelty of the new approach is its insensitivity to~~  
366 ~~the mean Doppler velocity, which is  $\sigma$ , especially at Punta Arenas  $\sigma$ , strongly influenced by orographic mountain waves,~~  
367 ~~because. Instead, it uses the radar reflectivity factor, skewness and the edge width of the Doppler spectrum is used instead.~~

369 The PROM-project *Investigating the impact of Land-use and land-cover change on Aerosol-Cloud-precipitation*  
370 *interactions using Polarimetric Radar retrievals (ILACPR)* ~~analyzes a will provide new insights on the impact of~~  
371 ~~anthropogenic land use and land cover changes on precipitating cloud structure and its dynamics. A co-analysis of polarimetric~~  
372 ~~radar observations and model simulations simultaneous in order to improve our understanding of is used to investigate~~  
373 ~~interactions between land-aerosol-cloud-precipitation interactions processes. The fusion of radar observations and models with~~  
374 ~~the aid of forward operators, allowed, which will allow us to interrogate the effects of anthropogenic interventions on~~  
375 ~~precipitation generating processes and the capabilities of numerical models to reproduce them. The Terrestrial Systems~~  
376 ~~Modelling Platform (TSMP; Shrestha et al., 2014; Gasper et al., 2014) developed under by the DFG-funded Transregional~~  
377 ~~Research Center TR32 (Simmer et al., 2015) is was used to simulate a hailstorm observed on 5 July 2015 to simulate multiple~~  
378 ~~summertime convective storms passing with the polarimetric X-band radar (BoXPOL, e.g. Diederich et al., 2015a,b) located~~  
379 ~~over passing the city of Bonn, Germany. TSMP was found to generally underestimates the convective area fraction, high~~  
380 ~~reflectivities, and the width/magnitude of so-called differential reflectivity (ZDR) columns indicative of updrafts, all leading~~  
381 ~~to an underestimation of the frequency distribution for high precipitation values (Shrestha et al., 2021a). A decadal scale~~  
382 ~~simulation over the region using the hydrological component of TMSP also showed that much of the variability in the~~  
383 ~~simulated seasonal cycle of shallow groundwater could be linked to the distribution of clouds and vegetation (Shrestha, 2021),~~  
384 ~~which further. This additionally emphasizes the importance of model evaluation into representing clouds and precipitation~~  
385 ~~processes. The fusion of radar observations and models with the aid of observation forward operators, allowed for an extended~~  
386 ~~us to further interrogation of interrogate the effects of anthropogenic interventions on precipitation generating processes and~~  
387 ~~the capabilities of numerical models to reproduce them. Here, we basically show case findings from one a simulated hailstorm~~  
388 ~~observed on 5 July 2015 passing the city of Bonn, Germany are explained. Sensitivity simulations are were conducted using~~  
389 ~~large-scale aerosol perturbations and different land-cover types reflecting actual, reduced and enhanced human disturbances.~~  
390 ~~While the differences in modelled precipitation in response to the prescribed forcing are were below 5 %, the micro- and~~  
391 ~~macrophysical pathways are were found to differ, acting as a buffered system to the prescribed forcings (Stevens and Feingold,~~  
392 ~~2009; Seifert and Beheng, 2012). Fig. 5 shows vertical cross-sections reconstructed from volume scans measured with BoXPOL~~  
393 ~~together with simulated  $Z_H$  and  $Z_{DR}$  for the TSMP simulations with actual land-cover but perturbed condensation nuclei (CN)~~

394 and ice nucleating particle (INP) concentrations. CN concentrations are  $100 \text{ cm}^{-3}$  for maritime and  $1700 \text{ cm}^{-3}$  for continental  
395 aerosol. Similarly, concentrations for dust, soot and organics are  $162\text{E}3 \text{ m}^{-3}$ ,  $15\text{E}6 \text{ m}^{-3}$  and  $177\text{E}6 \text{ m}^{-3}$ , respectively, for default  
396 INP. For low/high INP, the concentration of soot and organics are decreased/increased by one order of magnitude. To generate  
397 the synthetic radar observations (The Bonn Polarimetric Radar observation forward Operator, B-PRO, (Xie et al., 2021; Xie et  
398 al., 2016; Heinze et al., 2017; Shrestha et al., 2021b) is/was has been applied. B-PRO is based on the an early fork of the \_based  
399 on an early, non-polarimetric version of EMVORADO (Zeng et al., 2016); and expands its code part for computing  
400 unattenuated radar reflectivity on the original model grid (Blahak, 2016) has been expanded to unattenuated polarimetric  
401 variables based on spheroidal shape assumptions (T-matrix), and further developed within the *Operation Hydrometeors*  
402 project jointly with the polarimetric version of EMVORADO (Mendrok et al., 2021; see also Sect. 3.1) has been applied to  
403 generate the synthetic variables. Because the full polarimetric version of EMVORADO Since (Pol-(Pol-EMVORADO, see)  
404 as described below in Section 4.1) was only released very recently, the model data in ILACPR this sub-project has been/was  
405 processed using B-PRO. Preliminary comparisons between B-PRO and recently available Pol-EMVORADO (notw shown  
406 here) exhibit negligible differences in their results on the model grid, but Pol-EMVORADO is/would have been much more  
407 computationally efficient and would have allowed to takes effects of beam broadening and attenuation along the actual radar  
408 ray paths into account. The vertical cross sections are compared at different times marked by the vertical grey bars in the time  
409 series of Convective Area Fraction (CAF, Fig. 5 a), defined as the ratio of area with  $Z_H > 40 \text{ dBZ}$  (at  $2 \text{ km a.g.l.}$ ) to total storm  
410 area. On average BoXPol observations show a bit higher CAF compared to the simulations. The evolution is always similar in  
411 terms of an initial increase and intensification in the second part of the observation period, where the experiment with maritime  
412 aerosols and low INP (Mar-lowIN) is closest to the observations. All simulations show  $Z_H$  and  $Z_{DR}$  patterns comparable to  
413 BoXPol observations, however, the experiment with continental aerosol and default INP (Con-defIN, Fig. 5c) shows weaker  
414  $Z_H$ , while Mar-lowIN (Fig. 5d) shows somewhat a bit higher  $Z_H$  values compared to BoXPol (see Fig 5a). The simulations with  
415 maritime CN produce low cloud droplet concentrations with relatively larger mean diameters compared to the simulations with  
416 continental CN. Accompanied by a very strong updraft, this also leads/leads to high concentrations of supercooled raindrops  
417 above the melting layer with broader spatial extent (due to a broader updraft region) compared to the simulations with  
418 continental CN simulations and. This contributes to an enhanced growth of hail, producing larger hail particles compared to  
419 the continental runs, resulting in higher  $Z_H$ . Also, as shown in the time-series of the CAF, simulations with continental aerosol  
420 and default/high IN tend to exhibit similar behaviour in radar space, with the latter exhibiting higher CAF only at latter stages  
421 of the storm. The continental CN simulations with default and high IN differ in terms of simulated updraft speed and total  
422 hydrometeor content, being higher for the latter one. However, Cont-highIN produces smaller graupel and hail particles  
423 compared to Cont-defIN, resulting in similar  $Z_H$ . CN concentrations are  $100 \text{ cm}^{-3}$  for maritime and  $1700 \text{ cm}^{-3}$  for continental  
424 aerosol. Similarly, concentrations for dust, soot and organics are  $162\text{E}3 \text{ m}^{-3}$ ,  $15\text{E}6 \text{ m}^{-3}$  and  $177\text{E}6 \text{ m}^{-3}$ , respectively, for default  
425 INP. For low/high INP, the concentration of soot and organics are decreased/increased by one order of magnitude. The  
426 experiment with continental aerosol and high INP concentration (Con-highIN, not shown) generates similar polarimetric  
427 moments to the Con-lowIN. All experiments exhibit/show vertically extensive columns of (slightly) enhanced  $Z_{DR}$ , collocated

Formatiert: Hochgestellt

Formatiert: Hochgestellt

Formatiert: Hochgestellt

Formatiert: Hochgestellt

Formatiert: Hochgestellt

428 with intense simulated updrafts reaching up to 13 to 14 km height. Indeed, these  $Z_{DR}$  -columns emerged recently as proxies  
429 for updraft strength and ensuing precipitation enhancement (Weissmann et al., 2014; Simmer et al., 2014; Kumjian et al., 2014;  
430 Kuster et al., 2020), and research on their exploitation for nowcasting and data assimilation is ongoing. In Fig. 5c/d synthetic  
431  $Z_{DR}$ -columns are vertically extensive, while  $Z_{DR}$  values within the column stay below 0.3 dB. BoXPOL observations show  $Z_{DR}$   
432 -columns reaching up to 6 km height only but with  $Z_{DR}$  values exceeding 1dB. While  $Z_{DR}$  values in the lower part of the  
433 columns are mostly generated by large raindrops, freezing drops and wet hail determine  $Z_{DR}$  in the upper parts of the column  
434 (Kumjian et al., 2014; Snyder et al., 2015). The diverging appearance of observed and synthetic  $Z_{DR}$  columns may point to a  
435 deficiency in the treatment of raindrops undergoing freezing and motivates further research. Too rapid freezing of drops  
436 combined with graupel generated from the frozen drops may generate enhanced but still low  $Z_{DR}$  up to high altitudes. Following  
437 Ilotoviz et al. (2018) such attributes of  $Z_{DR}$  columns are highly determined by the vertical velocity, hail size, and aerosol  
438 concentration, e.g. higher CN concentrations lead to higher columns with higher  $Z_{DR}$  values inside and also higher  $Z_H$ . In this  
439 case study and the specific time step shown, Mar-lowIN (i.e. with lower CN concentration) shows a wider and somewhat a bit  
440 taller  $Z_{DR}$  column together with a more intense  $Z_H$  core (compare Fig. 5c/d). Further explanations, however, require an  
441 improved representation of the  $Z_{DR}$ -columns in the model.

#### 442 4 Fusion of radar polarimetry and atmospheric models

443 Probably the most important and central tool for connecting polarimetric observations with numerical atmospheric models are  
444 observation operators, which generate virtual observations from the model state. These virtual observations can be  
445 directly compared with the real observations and signatures of microphysical processes including their temporal evolution.  
446 Thus, the accuracy of precipitation and cloud parameterizations can be indirectly evaluated  
447 and a database established for model optimization. Missing polarimetric process fingerprints (e.g. Kumjian, 2012) in the virtual  
448 observations may hint at model deficiencies, and model parameterizations can be adapted  
449 in order to increase the coherence between real and virtual observations. Moreover, sufficiently accurate and fast observation  
450 operators are mandatory for the direct assimilation of observations using ensemble methods.

451 However, bulk cloud microphysical parameterizations required for NWP models include  
452 assumptions on several critical parameters and processes to make up for lacking constraints from which are not explicitly  
453 prognosed- respectively resolved by the governing numerical model. An example are the inherently assumed particle size  
454 distributions and their relations to the prognostic moments (hydrometeor mass- and number densities). Another challenge is  
455 the handling of hydrometeor parameters that which are insufficiently or not at all unconstrained by the model's microphysics  
456 but are highly relevant for the calculation of virtual observations in the (radar) observation forward operator. For example, the  
457 melting state as well as in most operational bulk schemes the melting state as well as shape, microstructure, and spatial and  
458 orientation and melting state of the different hydrometeors are not prognostic (or not even implicitly assumed) in most  
459 operational bulk schemes. Therefore, suitable, so that, as a way out, meaningful. These assumptions need also to be made

Formatiert: Schriftart: Nicht Fett

Formatiert: Schriftart: Nicht Fett

Formatiert: Schriftart: Nicht Fett

Formatiert: Schriftart: Nicht Fett

Formatiert: Schriftart: Nicht Fett

Formatiert: Schriftart: Nicht Fett

Formatiert: Schriftart: Nicht Fett

Formatiert: Schriftart: Nicht Fett

460 taken into account in observation operators in order to create meaningful virtual observations. For example, in most  
461 operational bulk schemes the melting state as well as shape, microstructure, and orientation of the different hydrometeors are  
462 not prognostic (or not even implicitly assumed). These assumptions need also to be taken into account in observation operators  
463 in order to create meaningful virtual observations. An example are the inherently assumed particle size distributions and their  
464 relations to the prognostic moments. Moreover, bulk cloud microphysical schemes may only insufficiently approximate the  
465 natural variability, and the interactions between the few small sets of assumed hydrometeor classes, and the size distribution  
466 moments that are mainly tuned to get, e.g., the surface precipitation right. Therefore, these current approximations in both  
467 numerical models and observation operators may hence translate into different sources of errors and biases of the simulated  
468 radar variables (e.g. Schinagl et al., 2019; Shrestha et al., 2021b). As an example can be seen in, Figure 7 shows too low  
469 polarimetric signals above the melting layer, which are partly caused by assumptions inherent in the observation forward  
470 operator will be discussed in (see Sect. 4.2.1). Such problems challenge both model evaluation and data assimilation. The  
471 central science questions are therefore the realism of the sensitivities of simulated radar variables to parameters in the  
472 observation operators and the models, as well as and the effective approaches to the evaluation and improvement of moist  
473 processes parametrizations.

474 Another challenge problem for large-scale applications such as like long-term model evaluations or operational real-time data  
475 assimilation based on large radar networks is the high computational demand and low speed of that current polarimetric radar  
476 observation operators are often much too slow and computationally expensive and much too slow. Often, the operators apply  
477 some kind of pre-calculated lookup tables (LUT) of scattering properties and as well as parallelization techniques for speed  
478 optimizations (e.g. Wolfensberger and Berne, 2018; Matsui et al., 2019; Oue et al., 2020). Despite that, radar simulations for  
479 a single timestep take - depending on the computer - on the order of minutes for one single plan position indicator (PPI)  
480 elevation scan (Wolfensberger and Berne, 2018) or for a single model scene (CR-SIM; Oue et al., 2020). Matsui et al. (2019)  
481 state the LUT generation process of their POLARRIS-f operator to only take a few take few minutes when distributed to few  
482 thousands of processors, but do not elaborate on the required times for the actual simulation of the radar measurement. For  
483 example, to simulate one single PPI elevation for one radar station and one time step, the research type operator of  
484 Wolfensberger and Berne (2018) takes on the order of 5 to 10 minutes, depending on the computer, which means that PPI  
485 volume scans with several elevations for large networks of stations would take several hours! The operator CR-SIM (Oue et  
486 al., 2020) for simulations of polarimetric moments on the NWP model grid (no PPIs or volume scans) is of comparable  
487 efficiency. Both operators are somehow speed optimized by making use of code parallelization and lookup tables for single  
488 particle scattering properties. The operator B-PRO (Xie et al., 2016), which uses neither of these techniques, is much slower,  
489 as experienced in during applications within during phase 1 of SPP-PROM have demonstrated (Shrestha et al., 2021b). While  
490 acceptable for research, real-time operational applications may pose much stricter time constraints. Therefore, an important  
491 technical goal is to provide an efficient, (yet physically accurate and “state-of-the-art”) polarimetric radar operator to the  
492 community, which reduces the simulation time for multi-elevation PPI volume scans of many stations to a few seconds.

#### 4.1 Polarimetric Radar observation operator developments

Within the PROM-project *Operation Hydrometeors*, the up-to-now non-polarimetric radar observation operator EMVORADO (Zeng et al., 2016; Blahak and de Lozar, 2020; Blahak, 2016) has been extended to polarimetry (Mendrok et al., 2021) called Pol-EMVORADO in the following.

(Non-polarimetric) EMVORADO has been designed to efficiently simulate PPI volume scan measurements of entire radar networks from the prognostic model state of an NWP model. PPI volume scans can be simulated for many radar stations simultaneously for direct comparisons with the radar observations. EMVORADO is part of the executable of both the COSMO and ICON NWP models, which allows allowing to run the operator within a NWP model run and executable and to access the model state and radar variables in memory. The code is MPI- and OpenMP-parallelized and thus fully exploits the computational power of modern HPCs and avoids storing and re-reading extensive model state data to/from hard drives. This enables large-scale real-time applications such as operational data assimilation and extensive NWP model verifications using whole radar networks at high temporal resolution. Its modular nature allows for relatively easy interface development to other NWP models. An offline framework is also available, which accesses model states of one model time step from harddisk. EMVORADO includes detailed modular schemes to simulate beam bending, beam broadening and melting effects, and allows users to choose for each process between computationally cheap and physically accurate options. The operator has been used for the assimilation of radar reflectivity with positive impact on precipitation forecasts (Bick et al., 2016; Zeng et al., 2018, 2019, 2020). Currently, DWD uses EMVORADO to operationally assimilate 3D volumetric reflectivity and radial wind observations of its C-Band radar network. Key for this application is also the extensive use of precomputed lookup tables which that relate (Mie-theory based) bulk reflectivity directly to hydrometeor densities and temperature. The effects of neglecting radar beam pattern and reflectivity weighting, beam broadening and of hydrometeor fall speeds on data assimilation have been investigated in a joint effort together with the PROM-project *Representing model error and observation Error uncertainty for Data assimilation of Polarimetric radar measurements (REDPOL)* (Zeng et al., 2021a).

The polarimetry-extended Pol-EMVORADO, in the following referred to as Pol-EMVORADO, has inherited all features of EMVORADO, which in turn have been and expanded them where necessary to calculate and handle polarimetric observables/variables. This includes, e.g., the different beam bending, beam broadening, and beam smoothing schemes, the effective medium approximations allowing 1- and 2-layered hydrometeors with different water-ice-air mixing schemes and melting topologies, and the lookup table approach for an efficient access to polarimetric observables such as  $Z_{DR}$ , LDR,  $\rho_{HV}$ , and  $K_{DP}$ . Optionally, attenuation effects can be considered, and specific and differential attenuation ( $A_H$  and  $A_{DP}$ , respectively) provided, can be considered and further output quantities derivable from the complex scattering amplitudes can easily be added. Pol-EMVORADO applies state-of-the-art State-of-the-art S scattering properties of spheroidal particles derived by one-layered (Mishchenko, 2000) and two-layered T-Matrix approaches (Ryzhkov et al., 2011) are used instead of the "spherical" Mie theory used in EMVORADO. Assumptions on spheroid shape and orientation follow parametrizations introduced in Ryzhkov et al. (2011). The lookup table approach has been revised to accommodate the additional parameters necessary to derive the



527 full set of polarimetric radar output. ~~For a given set of parameters affecting the hydrometeor scattering properties, the lookup~~  
528 ~~tables are created only once, stored in files, and are re-used for subsequent runs.~~

529 ~~Using With the use of pre-existing lookup tables, the computations for virtual simulated polarimetric volume scans of radar~~  
530 ~~networks are very fast. For example, on a Linux PC with 8 cores it takes only about 10 seconds to simulate the volume~~  
531 ~~scans observations of all polarimetric parameters for all 176 German radars takes a few seconds only on a Linux~~  
532 ~~workstation (8 cores) and adds only about 1 s per radar output timestep to the model runtime when performed of all 16 German~~  
533 ~~radars for one time of day and all polarimetric moments. Simulating these volume scans online during an run of ICON-D2 run~~  
534 ~~(DWD's operational convection-allowing ICON version with 2 km grid spacing) on DWD's NEC Aurora supercomputer. That~~  
535 ~~is, adds only about 1 s per radar output time to the model runtime. If radar data are simulating polarimetric radar data in~~  
536 ~~intervals of 5 min as observed by DWD's weather radar network, this adds up to only a few percent more total model runtime~~  
537 ~~(Mendrok et al., 2021) making it possible feasible to run Pol-EMVORADO for assimilation of high temporal resolution~~  
538 ~~polarimetric radar data in an operational framework.~~

539 Pol-EMVORADO ~~has been is now~~ incorporated into the official version of EMVORADO and can be run ~~online (i.e. within~~  
540 ~~a COSMO or ICON run) as well as~~ offline (i.e. stand-alone with model fields from data files) ~~and online (i.e. within a COSMO~~  
541 ~~or ICON run). Although designed as a PPI volume scan observation operator for a radar network, its output can also be~~  
542 provided on NWP model grids. An example of a ~~synthetic Z<sub>DR</sub> volume scan simulated by Pol-EMVORADO for from the~~  
543 ~~REDPOL project is shown given in Fig. 6 (see also Sect. 4.2.3).~~

544 ~~In summary, (Pol-)EMVORADO comprises a wide set of state-of-the-art features. While each of these features is provided~~  
545 ~~also by other observation forward operators, to our knowledge, (Pol-)EMVORADO is, to our knowledge, unique in combining them into an~~  
546 ~~operator that allows to simulate virtual observations, including instrumental effects and in formats directly comparable to real~~  
547 ~~observational scans, from within NWP model runs in a comparably accurate and very fast manner targeted at operational~~  
548 ~~applications. Mendrok et al. (2021) give a comprehensive description of the features developed or updated for Pol-~~  
549 ~~EMVORADO including details on their implementation and performance.~~

550 ~~From the application of During application of Applying Pol-EMVORADO (or the related B-PRO, see Sect. 3.2) within~~  
551 ~~PROM, a number of several problems issues became evident. Modeling Assuming hydrometeors as homogeneous effective-~~  
552 ~~medium particles (e.g. oblate spheroids) does not reproduce well the polarimetric signatures of low density hydrometeors like~~  
553 ~~dendrites or aggregates as typical for snow while keeping their microphysical properties (e.g. aspect ratio, degree of~~  
554 ~~orientation) within realistic - observed or model-predicted - ranges and consistent between different radar frequencies. This~~  
555 ~~deficiency has been demonstrated and explained from electromagnetic theory by Schrom et al. (2018). It is obvious and became~~  
556 ~~also evident in our the case study (by Shrestha et al., (2021b) and in Fig. 7 shown here, where Z<sub>DR</sub> and K<sub>DP</sub> in the snow-~~  
557 ~~dominated layer between 2.5 and 5 km height almost entirely lack the typical observed features in the snow-dominated layer~~  
558 ~~between 2.5 and 5 km height, i.e. bands of enhanced Z<sub>DR</sub> and K<sub>DP</sub> in the DGL and dendritic growth layer that then smoothly~~  
559 ~~decreasing to mostly positive, non-zero values towards downwards to the melting layer. This deficiency can also be observed~~  
560 ~~with other polarimetric observation operators FOs applying a T-matrix approach (see simulation-to-observation comparisons~~

561 ~~in Wolfensberger and Berne (2018), Matsui et al. (2019), Oue et al. (2020), where the lack of ZDRZDR and KDP KDP~~  
562 ~~signatures is not discussed at all or exclusively explained by lack of secondary ice, though), which nevertheless currently~~  
563 ~~constitutes the state-of-the-art in radar polarimetry.~~ Orientation and shape of frozen and melting hydrometeors are very  
564 variable, both in nature and in the assumptions used in observation operators, which translates into large uncertainties in  
565 polarimetric radar signatures (e.g., Matsui et al., 2019; Shrestha et al., 2021b).

566 -To tackle these challenges, ~~it is planned to Pol-EMVORADO will be interfaced~~ Pol-EMVORADO ~~include in the future~~  
567 ~~interfaces to several~~ scattering databases or other scattering models in order to enable more realistic cloud ice and aggregate  
568 snowflake scattering properties and allow for improvements or extensions of the polarimetry-related microphysical  
569 assumptions (shape/habit/microstructure, orientation and their distribution, e.g., Wolfensberger et al., 2018), particularly for  
570 (partly-)frozen hydrometeors. ~~For This will be taken up in~~ PROM's 2<sup>nd</sup> phase, ~~we have proposed to take this up~~ guided with  
571 Lagrangian particle model information, as well as ~~to the~~ test ~~the application~~ of Pol-EMVORADO in an operational data  
572 assimilation environment.

## 573 4.2 Model evaluation and improvements using forward simulations and microphysical retrievals

### 574 4.2.1 Convection-resolving simulations with COSMO

575 In a joint effort, the PROM-projects *Operation Hydrometeors* and *ILACPR* evaluated simulated stratiform precipitation events  
576 in radar observation space and developed a sophisticated polarimetry-based hydrometeor classification and quantification for  
577 the evaluation of the representation of hydrometeors in numerical models. Based on a stratiform event monitored on 7 October  
578 2014 with the Bonn polarimetric X-Band radar BoXPoL, Fig. 7 illustrates the potential of using polarimetric observations for  
579 the evaluation and improvement of microphysical ~~parametrizations~~parametrisations. Fig. 7 a-f compare QVPs of measured  
580 and virtual  $Z_H$ ,  $Z_{DR}$ , and  $K_{DP}$  with the Bonn Polarimetric Radar ~~observationforward~~ Operator B-PRO (Xie et al., 2021) to  
581 forecasts simulated with COSMO version 5.1 using its 2-moment cloud microphysics scheme (itype\_gscp=2683; Seifert and  
582 Beheng, 2016). Due to a small spatial shift of the precipitation event in the simulations, the observations at 50.7305 N, 7.0717  
583 E are compared with simulations at a close-by grid\_point at 51.1 N, 7.0717 E. As demonstrated in Shrestha et al. (2021b)  
584 using a similar stratiform precipitation event, COSMO tends to simulate considerable amounts of melting graupel partly  
585 reaching the surface, which results ~~within and below the melting layer (ML) in~~ to higher synthetic  $Z_{DR}$  than observed (compare  
586 Fig. 7c/d) ~~within and below the melting layer (ML)~~. Above the ML, however, synthetic  $Z_{DR}$  already approaches 0-0 dB at  
587 around 6 km height, which indicates deficiencies in the ice-snow partitioning in COSMO ~~as well as in the assumed snow~~  
588 ~~morphology and the approximation of snow particles as~~ (soft spheroids) in ~~the observationforward operator~~B-PRO ~~leading,~~  
589 ~~both resulting~~ in too low polarimetric signals. While ~~the~~ observed and simulated  $Z_H$  is comparable in terms of structure and  
590 magnitude, ~~except a more pronounced observed ML,~~ larger differences exist with respect to  $K_{DP}$  above the ML (Fig. 7e/f).  
591 While observations show bands of enhanced  $K_{DP}$  within the ~~so-called~~ dendritic growth layer (DGL) centred around  $-15^{\circ}\text{C}$ ,  
592 the simulated  $K_{DP}$  is very weak indicating a lower crystal concentration and early aggregates compared to observations (e.g.  
593 Moisseev et al., 2015). ~~I~~Comparison of ice water content (IWC) above the ML retrieved from measured  $K_{DP}$  and differential

594 reflectivity in linear scale  $Z_{dr}$ , i.e.  $IWC(K_{DP}, Z_{dr})$  following Ryzhkov et al. (2018), ~~agrees well with IWC modelled by the~~  
595 COSMO ~~simulated IWC agrees well~~ in terms of structure, but has lower magnitudes (compare Fig. 7 g/h) in line with the lower  
596 simulated  $K_{DP}$ . Overall, Fig. 7 supports the hypothesis of a too strong graupel production in ~~the simulations~~. **Operation**  
597 **Hydrometeors** also developed a robust radar-based hydrometeor classification (HMC) and mixing ratio quantification  
598 algorithm following Grazioli et al. (2015) and Besic et al. (2016, 2018) for the evaluation of the representation of hydrometeors  
599 in NWP models (standard output is the dominant hydrometeor type only). ~~This HMC is based on clustering and has the~~  
600 ~~advantage that the radar data are separated into clusters based on their polarimetric similarity (no theoretical preliminary~~  
601 ~~calculation is needed), which are then identified as hydrometeor classes. Various~~~~This type of HMC can be used with different~~  
602 ~~clustering methods can be used here (e.g. Lukach et al. (2021)).~~ The new method is relatively insensitive to uncertainties in  
603 the scattering properties of ice particles. Its application to the BoXPoL observations above does not indicate graupel below the  
604 ML (Fig. 8a), while COSMO simulates a pronounced, thick graupel layer (Fig. 8b) including some melting graupel particles  
605 reaching the ground around 1:45 UTC. ~~Applying the HMC, which is based on clustering, to the virtual observations, however,~~  
606 ~~it does not reproduce a graupel layer of similar intensity (Fig. 8c), probably caused by a too strong  $Z_H$  and temperature influence~~  
607 ~~(compare with Fig. 7) relative to the polarimetric variables in the classification scheme which needs further investigation. A~~  
608 ~~persistent challenge in according routines is that clusters are always separated by the 0°C-level (e.g. Ribaud et al., 2019), i.e.~~  
609 ~~hail or graupel are identified as clusters only below or above the melting layer. Applied to the virtual observations, however,~~  
610 ~~does not reproduce a graupel layer of similar intensity (Fig. 8c), probably caused by a too strong  $Z_H$  and temperature influence~~  
611 ~~(compare with Fig. 7) relative to the polarimetric variables in the classification scheme which needs further investigation. For~~  
612 the case study in Shrestha et al. (2021b) the simulated graupel was even more pronounced and sensitivity experiments were  
613 performed to guide model improvement: ~~Increasing the minimum critical particle diameter  $D_{crit}$ , which is required for self-~~  
614 ~~collection of ice particles (aggregation) increased/improved the ice-snow partitioning, and a lower temperature threshold for~~  
615 ~~snow and ice riming,  $T_{ime}$ , considerably reduced the graupel production.~~  
616 Comparing state-of-the-art polarimetric retrievals of liquid water content (LWC), ice water content (IWC), particle number  
617 concentration  $N_t$  and mean particle diameter  $D_m$  (e.g. Ryzhkov et al., 2018; Ryzhkov and Zmic, 2019; Bukovčić et al., 2020;  
618 Reimann et al., 2021; Trömel et al., 2019) with their simulated counterparts can also be used for evaluating NWP models and  
619 for data assimilation (Carlin et al., 2016). Fig. 7g/h, e.g., shows higher  $IWC(K_{DP}, Z_{dr})$  than simulated by COSMO for the case  
620 study discussed earlier. For more solid conclusions about possible model errors, ~~as well as—and~~ for the use of retrieved  
621 quantities for data assimilation, the retrieval uncertainties must be estimated. The analysis of data collected in the ice regions  
622 of tropical convective clouds indicates e.g., that  $IWC(K_{DP}, Z_{dr})$  yields a root-mean-square error of ~~of~~  $0.49 \text{ gm}^{-3}$  with the bias  
623 within 6% (Nguyen et al., 2017; 2019). ~~Murphy et al. (2020) introduced the columnar vertical profile (CVP) methodology to~~  
624 ~~follow the track of research aircrafts and better co-locate in-situ data to radar microphysical retrievals. Applying the~~  
625 ~~methodology to two mesoscale convective systems, they found the best performance of polarimetric microphysical retrievals~~  
626 ~~in regions of high ZDR and high KDP but recommend a much larger dataset to fully conclude on the accuracy of these~~  
627 ~~retrievals.~~

628

629 The PROM-project *POL*arimetric signatures of *ICE*ee microphysical processes and their interpretation using in-situ  
630 *observations and cloud modelling (POLICE)* evaluates radar retrievals and models using in particular in-situ observations of  
631 microphysical cloud parameters from the research aircrafts HALO (e.g. Wendisch et al., 2016; Voigt et al., 2017) and Falcon  
632 (e.g. Voigt et al., 2010; Voigt et al., 2014; Flamant et al., 2017). Currently, ground-based polarimetric radar measurements and  
633 aircraft in-situ data from the Olympic Mountain Experiment OLYMPEX (Houze et al., 2017; Heymsfield et al., 2018) are  
634 exploited to investigate riming processes and to evaluate retrievals of ice water content (IWC), particle number concentration  
635  $N_t$ , and mean particle diameter  $D_m$  (e.g. Ryzhkov et al., 2018; Ryzhkov and Zrnica, 2019; Bukovčić et al., 2020; Carlin et al.  
636 2021). The OLYMPEX mission took place on the Olympic Peninsula of Washington State (USA) from November 2015  
637 through February 2016. ~~The research science aircraft~~ University of North Dakota's (UND) Cessna Citation II equipped with  
638 an in-situ cloud payload overpassed the National Science Foundation (NSF) Doppler On Wheels (DOW, mobile polarimetric  
639 X-band radar with about 60 km range and 74 m radial resolution), placed in the Chehalis Valley at Lake Quinault (47.48° N,  
640 123.86° W, 64 m altitude) performing RHI scans within an azimuthal sector of 22°. Measurements and microphysical retrievals  
641 of the DOW and the Citation, respectively, are currently evaluated and will then be compared at matched space-time  
642 coordinates for several flight transects.

643

#### 644 4.2.2 Climate simulations with ICON-GCM

645 A major part of the uncertainties in representing clouds and precipitation in atmospheric models can be attributed to unresolved  
646 variability that affects resolved variables via non-linear processes. Current climate model horizontal resolutions are ~~on~~  
647 the order of 100 km. But even for NWP models, which have resolutions between 10 km for global and 1 km for regional  
648 simulations, most cloud processes remain unresolved. The project *Climate model P*arameterizations informed by *R*adar  
649 (*PARA*) evaluates and improves the representation of cloud and precipitation processes in particular for climate models and  
650 focuses on precipitation formation in ice clouds. Since most surface precipitation over continents and extra-tropical oceans  
651 involve the ice phase (Mülmenstädt et al., 2015; Field and Heymsfield, 2015) its reliable representation is paramount and thus  
652 the focus of *PARA*. Microphysical ~~parameterizations~~~~parameterizations~~~~parameterizations~~ typically consider only the mean cloud  
653 liquid or ice water content to compute process rates, which causes biases in all ~~nonlinear~~~~non-linear~~ processes including  
654 radiation (e.g., Cahalan 1994; Carlin et al., 2002) and precipitation formation (e.g., Pincus and Klein, 2000). Realistic results  
655 thus require the tuning of process rates (e.g., Rotstayn 2000) or realistic estimates of subgrid-scale cloud variability and its  
656 inclusion in the process ~~parametrizations~~~~parameterizations~~. ~~To tackle this issue, PARA tries to exploit~~ ~~to this goal~~ inherent  
657 model assumptions for treating fractional cloudiness. Since the early works of Sommeria and Deardorff (1977), atmospheric  
658 models assume or predict some notion of subgrid-scale variability of relative humidity. Some models do so by predicting  
659 cloud fraction (e.g., Tiedtke 1993), others use a diagnostic representation of the subgrid-scale probability density function  
660 (PDF) of total water specific humidity,  $q_t$  (e.g., Sundqvist et al., 1989; Smith 1990; Le Treut and Li, 1991; Rosch et al., 2015).

661 Another option is to utilize a prognostic PDF of  $q_i$  by assuming a functional form and predicting the shape parameters of the  
662 PDF (e.g., Tompkins 2002; Neggers 2009). The German climate and weather prediction model ICON in its version dedicated  
663 to climate simulations (general circulation model version; ICON-GCM) inherits the representation of physical processes from  
664 its predecessor ECHAM6 (Stevens et al., 2013) and uses the Sundqvist et al. (1989) parameterization for a diagnostic PDF of  
665 the total-water specific humidity,  $q_i$ .

666 As a first step, PARA analyses the implied PDF of cloud ice using satellite observations from combined CloudSat-CALIPSO  
667 radar-lidar satellite observations (DARDAR, Delanoë et al., 2014). Interestingly, a first direct comparison of IWC profiles  
668 obtained from DARDAR with polarimetric retrievals based on the ground-based BoXPol radar shows an overall good  
669 agreement, except for columns with an integrated ice water path IWP  $> 1 \text{ kg m}^{-2}$ . In these regions pronounced polarimetric  
670 signatures result in high IWC at higher altitudes, which are neither reproduced by reflectivity-only retrievals nor by the  
671 DARDAR retrievals. The statistics are currently evaluated on a larger database, which is also used to investigate the impact  
672 on the [parametrizationsparameterizations](#) in ICON-GCM. In the second step, a stochastic parameterisation approach is taken  
673 to allow for an unbiased computation of cloud microphysical process rates on average. Based on the cumulative distribution  
674 function (CDF), a random number generator draws from the CDF according to the simulated likelihood a plausible value of  
675 the specific ice mass based on which the microphysical process is computed. This specifically considers the formation of solid  
676 precipitation (snow) from ice clouds via aggregation and accretion processes (Lohmann and Roeckner, 1996; Stevens et al.,  
677 2013), and subsequently the evaporation of precipitation below the clouds. The result of the revised aggregation  
678 [parametrizationsparameterization](#) is shown in Fig. 9. The increased aggregation rate, which is a [super-linear](#) function of the  
679 specific cloud ice,  $q_i$ , leads to an average decrease in  $q_i$ . The aggregation rate is directly linked to the accretion rate, which  
680 lowers the effect of  $q_i$  decrease. An investigation of the influence of the revised aggregation [parametrizationsparameterization](#)  
681 on the different microphysical process rates - which are related to the ice phase - is currently performed. A detailed evaluation  
682 of the new versus old [parametrizationsparameterizations](#) with [the](#) ground-based polarimetric radar is on its way, and will in  
683 particular focus on the time scales of evaporation of precipitation below the cloud.

#### 684 4.2.3 Data assimilation

685 Within an idealized framework, Jung et al. (2008, 2010) and Zhu et al. (2020) demonstrated benefits of assimilating simulated  
686 polarimetric data for the estimation of microphysical state variables. Up to now, however, direct assimilation of real  
687 polarimetric data poses great challenges due to the deficiencies of cloud and precipitation schemes in NWP models in  
688 realistically representing and providing the necessary information (optimally the distribution of particle size, shape and  
689 orientations in all model grid boxes) required by a polarimetric radar observation operator and therefore causing large  
690 representation error (Janjic et al., 2018). Both, [the](#) specification of model error to examine uncertainty in microphysics (Feng  
691 et al., 2021) and [the](#) specification of [the](#) observation error for polarimetric radar observations that include estimates of the  
692 representation error (Zeng et al., 2021b), [archave been](#) investigated in the PROM-project *REDPOL*. For the assimilation of

693 radar reflectivity with an ensemble Kalman filter, several approaches for including model errors during data assimilation  
694 ~~are~~ explored, including 1) additive noise with samples representing large-scale uncertainty (see Zeng et al., 2018), 2)  
695 combination of large scale and unresolved scale uncertainty (Zeng et al., 2019), and finally 3) adding to these warm bubble  
696 triggering of convective storms in case they are missing in the one hour forecast but present in corresponding observations  
697 (Zeng et al., 2020). Applying Pol-EMVORADO to the analysis obtained by assimilating radar reflectivity ~~from the~~(German  
698 C-Band network), Fig. 6 illustrates the resulting differences of these three techniques in  $Z_{DR}$ -space. Obviously, synthetic  $Z_{DR}$   
699 values depend on the strategy used to specify the model error, putting another weight to the argument that assimilation of radar  
700 reflectivity alone is not sufficient to constrain the estimation of microphysical state variables, and that polarimetric information  
701 is required in addition. First results in this direction were reported by Putnam et al. (2019), who assimilated  $Z_{DR}$  below the  
702 melting layer but reported problems in assimilation of  $K_{DP}$  data ~~for a supercell case due to high observation errors as a result~~  
703 ~~of contamination from wet hail, dust and debris and the potentially non-uniform beam filling.~~

## 705 5 Summary and Perspectives

706 The Priority Programme *Polarimetric Radar Observations meet Atmospheric Modelling (PROM)* (SPP 2115,  
707 <https://www2.meteo.uni-bonn.de/spp2115/>) was established in April 2017 by the Senate of the Deutsche  
708 Forschungsgemeinschaft (DFG, German Research Foundation) and is designed to run for six years. PROM is a coordinated  
709 effort to foster partnerships between cloud modelers and radar meteorologists and thus to accelerate the exploitation of  
710 polarimetric weather radars to improve the representation of cloud and precipitation processes in numerical models. The first  
711 funding phase engaged in an ~~as-complete-as-possible~~ exploitation and understanding of nation-wide polarimetric  
712 measurements complemented by state-of-the-~~art~~ measurement devices and techniques available at supersites. Bulk  
713 polarimetric measurements available over Germany are complemented with multi-frequency observations and spectral  
714 polarimetry for detailed studies of ice and cloud microphysics. Thus, ~~for the first time,~~ modellers ~~now hold an unprecedented~~  
715 ~~amount of~~ three-dimensional microphysics-related observational data in their hands to improve  
716 ~~parametrizations~~parameterisations. Key tools for the fusion of radar polarimetry and atmospheric modelling, e.g. the Monte-  
717 Carlo Lagrangian particle model McSnow and the polarimetric observation operator Pol-EMVORADO have been developed.  
718 PROM started with detailed investigations of the representation of cloud and precipitation processes in the COSMO and ICON  
719 atmospheric models exploiting ~~the~~polarimetric ~~B-PRO and EMVORADO~~ observation operators. First improvements of the  
720 2-moment cloud- and precipitation microphysics scheme are made and more are expected in phase 2. Also intercomparisons  
721 of microphysics schemes in radar space have been performed. Phase 1 further developed microphysical retrievals, determined  
722 their uncertainties and started their exploitation for model evaluation and radar-informed ~~parametrizations~~parameterizations.  
723 ~~The d~~Developed prerequisites pave the way to finally exploit polarimetry for indirect and direct data assimilation in the  
724 upcoming second funding phase.

725 Some tools developed in Phase 1, however, still require refinement in Phase 2. The T-matrix calculations for  
726 electromagnetic scattering by spheroidal particles represent only a crude approximation to frozen and mixed-phase  
727 hydrometeors, especially for pristine ice particles and aggregate snowflakes at cloud radar wavelengths. It is not possible to  
728 reproduce observed polarimetric signatures of snow with the T-Matrix approach (i.e. homogeneous ice-air spheroids) and  
729 realistic microphysics (shape, orientation). Refinements include interfacing to a new discrete dipole approximation (DDA)-  
730 based scattering data base for realistic ice and snow particles for all relevant weather radar wavelengths and improvements of  
731 the melting scheme of graupel and hail.

732 Based on the [progress made](#), ~~made progress~~ the fusion of radar polarimetry and atmospheric modelling can be approached even  
733 more aggressively in Phase 2. While objective 1 received most attention in Phase 1, more projects will exploit ~~now~~ the  
734 observational insights and tools developed to finally improve parameterizations and assimilate polarimetric information, i.e.  
735 more emphasis will be put on Objectives 2 and 4 in Phase 2. Direct assimilation of polarimetric variables remains challenging,  
736 because NWP models need to realistically represent and provide the necessary information required by a polarimetric radar  
737 observation operator; ideally the distribution of particle size, shape and orientation would be required in all model grid boxes.  
738 Indirect assimilation of polarimetric information (e.g. microphysical retrievals, and process signatures), however, is less  
739 demanding to the model and should be pursued in parallel. Modern Bayesian data assimilation techniques are sensitive to both  
740 model- and [observation](#)~~forward~~ operator biases, so that further work on these issues is of great importance for a successful  
741 data assimilation.

742

#### 743 **Data availability**

744 The data presented in this paper are available through the authors upon request. Polarimetric radar data from the operational  
745 C-band radar network is also available from the German Weather Service (DWD). Specific campaign data will be published  
746 in addition.

747

#### 748 **Author contributions**

749 Silke Trömel had the initial idea and mainly organized and structured the joint publication. Silke Trömel, Johannes Quaas, and  
750 Clemens Simmer formed the editorial team consolidating the text. All authors contributed to specific sections of the paper and  
751 commented on the paper.

752

#### 753 **Competing interests**

754 Johannes Quaas is editor of ACP. The authors declare to have no additional conflict of interest.

755

#### 756 **Special issue statement**

757 This article is the overview article of the ACP/AMT/GMD inter-journal special issue “Fusion of radar polarimetry and  
758 numerical atmospheric modelling towards an improved understanding of cloud and precipitation processes”. It is not associated  
759 with a conference.  
760

#### 761 Acknowledgments

762 We gratefully acknowledge the funding of the German Research Foundation (DFG) to initialize the special priority program  
763 on the Fusion of Radar Polarimetry and Atmospheric Modelling (SPP-2115, PROM). The work of contributing authors was  
764 carried out in the framework of the projects Operation Hydrometeors (Grants TR 1023/16-1 and BL 945/2-1), [IcePolCKa \(HA](#)  
765 [3314/9-1 and ZI 1132/5-1\)](#), ILACPR (Grant SH 1326/1-1), IMPRINT (Grant KN 1112/3-1), POLICE (Grants TR 1023/13-1  
766 and VO 1504/5-1), PARA (Grants QU 311/21-1 and TR 1023/15-1), HydroColumn ([Grant FR 4119/1-1](#)), REDPOL (Grant JA  
767 1077/5-1), and PICNICC (Grants KA 4162/2-1 and SE 2464/1-1). [ILACPR gratefully acknowledges the computing time](#)  
768 [\(project HBN33\) granted by the John von Neumann Institute for Computing \(NIC\)](#)  
769 [and provided on the supercomputer JUWELS at Jülich Supercomputing Centre \(JSC\).](#)  
770

#### 772 References

773 Alfieria, L., Thielen, J., and Pappenberger, J.: Ensemble hydro-meteorological simulation for flash flood early detection in  
774 southern Switzerland, *J. Hydrol.*, 424, 143-153, doi:10.1016/j.jhydrol.2011.12.038, 2012.

775 Bauer, P., Thorpe, A., and Brunet, G.: The quiet revolution of numerical weather prediction, *Nature* 525, 47–55,  
776 doi:10.1038/nature14956, 2015.

777 Besic, N., Gehring, J., Praz, C., Figueras i Ventura, J., Grazioli, J., Gabella, M., Germann, U., and Berne, A.: Unraveling  
778 hydrometeor mixtures in polarimetric radar measurements, *Atmos. Meas. Tech.*, 11, 4847–4866, doi:10.5194/amt-11-4847-  
779 2018, 2018.

780 Besic, N., Figueras i Ventura, J., Grazioli, J., Gabella, M., Germann, U., and Berne, A.: Hydrometeor classification through  
781 statistical clustering of polarimetric radar measurements: A semisupervised approach. [Atmos. Meas. Tech. Atmospheric](#)  
782 [Measurement Techniques](#), 9(9), pp.4425-4445, 2016

783  
784 Bick, T., Simmer, C., Trömel, S., Wapler, K., Stephan, K., Blahak, U., Zeng, Y., and Potthast, R.: Assimilation of 3D-radar  
785 Reflectivities with an Ensemble Kalman Filter on the Convective Scale, *Quart. J. Roy. Meteor. Soc.*, 142, 1490–1504, 2016.  
786



787 Blahak, U.: RADAR\_MIE\_LM and RADAR\_MIELIB - Calculation of Radar Reflectivity from Model Output, COSMO  
788 Technical Report No. 28, Consortium for Small Scale Modeling (COSMO), available online [http://www.cosmo-  
790 model.org/content/model/documentation/techReports/docs/techReport28.pdf](http://www.cosmo-<br/>789 model.org/content/model/documentation/techReports/docs/techReport28.pdf), 2016.

791 Blahak, U. and De Lozar, A.: EMVORADO - Efficient Modular VOLUME scan RADAR Operator. A User's Guide, Deutscher  
792 Wetterdienst, available online [http://www.cosmo-model.org/content/model/documentation/core/emvorado\\_userguide.pdf](http://www.cosmo-model.org/content/model/documentation/core/emvorado_userguide.pdf),  
793 2020.

794

795 Brdar, S. and Seifert, A.: McSnow: A Monte-Carlo Particle Model for Riming and Aggregation of Ice Particles in a  
796 Multidimensional Microphysical Phase Space, *J. Adv. Model. Earth Syst.*, 10(1), 187–206, doi:10.1002/2017MS001167, 2018.

797

798 ~~Boucher, O., et al.: Clouds and aerosols, in *Climate Change 2013: The Physical Science Basis. Contribution of Working Group*  
799 *I to the Fifth Assessment Report of the Intergovernmental Panel on Climate Change*, edited by T. Stocker, et al., pp. 571–658,  
800 Cambridge University Press, Cambridge, United Kingdom and New York, NY, USA, 2013.~~

801

802 Bukovčić, P., Ryzhkov, A., and Zrnčić, D.: Polarimetric Relations for Snow Estimation—Radar Verification, *Journal of Applied*  
803 *Meteorology and Climatology*, 59(5), 991-1009, doi:10.1175/JAMC-D-19-0140.1, 2020

804

805 Bühl, J., Seifert, P., Wandinger, U., Baars, H., Kanitz, T., Schmidt, J., Myagkov, A., Engelmann, R., Skupin, A., Heese, B.,  
806 Klepel, A., Althausen, D., and Ansmann, A.: LACROS: The Leipzig Aerosol and Cloud Remote Observations System, in:  
807 *SPIE Remote Sensing*, edited by Comeron, A., Kassianov, E. I., Schäfer, K., Stein, K., and Gonglewski, J. D., p. 889002,  
808 Dresden, Germany, doi:10.1117/12.2030911, 2013.

809

810 Bühl, J., Seifert, P., Maygkov, A., and Ansmann, A. Measuring ice- and liquid-water properties in mixed-phase cloud layers  
811 at the Leipzig Cloudnet station, *Atmos. Chem. Phys.*, 16, 10609-10620, doi: 10.5194/acp-16-10609-2016, 2016

812

813 Cahalan, R. F.: Bounded cascade clouds: albedo and effective thickness, *Nonlinear Proc. In Geophysics.*, 1, 156-167, 1994.

814

815 Carlin, B., et al.: High-cloud horizontal inhomogeneity and solar albedo bias, *J. Climate*, 15, 2321 – 2339, 2002.

816

817 Carlin, J. T., Ryzhkov, A. V., Snyder, J. C., and Khain, A.: Hydrometeor Mixing Ratio Retrievals for Storm-Scale Radar Data  
818 Assimilation: Utility of Current Relations and Potential Benefits of Polarimetry, [Mon. Weather Rev. Monthly Weather Review](#)  
819 144(8), 2981-3001, doi:10.1175/MWR-D-15-461 0423.1., 2016.

820

821 [Carlin, J. T., Reeves, H. D., and Ryzhkov, A. V.: Polarimetric Observations and Simulations of Sublimating Snow:](#)  
822 [Implications for Nowcasting. J. Appl. Meteor. Climatol., 60\(8\), 1035-1054, doi:10.1175/JAMC-D-21-0038.1, 2021.](#)  
823

824 [Costa-Surós, M., Sourdeval, O., Acquistapace, C., Baars, H., Carbajal Henken, C., Genz, C., Hesemann, J., Jimenez, C., König,](#)  
825 [M., Kretzschmar, J., Madenach, N., Meyer, C. I., Schrödner, R., Seifert, P., Senf, F., Brueck, M., Cioni, G., Engels, J. F., Fieg,](#)  
826 [K., Gorges, K., Heinze, R., Siligam, P. K., Burkhardt, U., Crewell, S., Hoose, C., Seifert, A., Tegen, I., and Quaas, J.: Detection](#)  
827 [and attribution of aerosol–cloud interactions in large-domain large-eddy simulations with the ICOSahedral Non-hydrostatic](#)  
828 [model, Atmos. Chem. Phys., 20, 5657–5678, doi:10.5194/acp-20-5657-2020, 2020.](#)  
829

830 [Delanoë, J., Heymsfield, A. J., Protat, A., Bansemmer, A., and Hogan, R. J.: Normalized particle size distribution for remote](#)  
831 [sensing application, J. Geophys. Res. Atmos., 119, 4204-4227, doi:10.1002/2013JD020700, 2014.](#)  
832

833 [Diederich, M., Ryzhkov, A., Simmer, C., Zhang, P., and Trömel, S.: Use of specific attenuation for rainfall measurement at](#)  
834 [X-band radar wavelengths - Part 1: Radar calibration and partial beam blockage estimation, \*J. Hydrometeorol. Journal of\*](#)  
835 [Hydrometeorology](#), 16, 2, 487-502, doi: 10.1175/JHM-D-14-0066.1, 2015a.

836

837 [Diederich, M., Ryzhkov, A., Simmer, C., Zhang, P., and Trömel, S.: Use of specific attenuation for rainfall measurement at](#)  
838 [X-band radar wavelengths - Part 2: Rainfall estimates and comparison with rain gauges, \*J. Hydrometeorol. Journal of\*](#)  
839 [Hydrometeorology](#), 16, 2, 503-516, doi: 10.1175/JHM-D-14-0067.1, 2015b.

840

841 [Dipankar, A., Stevens, B., Heinze, R., Moseley, C., Zängl, G., Giorgetta, M., and Brdar, S.: Large eddy simulations using the](#)  
842 [general circulation model ICON, J. Adv. Model. Earth Sy., 7, 963–986, doi.org/10.1002/2015MS000431, 2015.](#)  
843

844 [Feng, Y., T. Janjic, Y. Zeng, A. Seifert, J. Min, 2021, Representing microphysical uncertainty in convective-scale data](#)  
845 [assimilation using additive noise, J. Adv. Model. Earth Sy., 2021 \(submitted\).](#)  
846

847 [Field, P. R. and Heymsfield, A. J.: Importance of snow to global precipitation, Geophys. Res. Lett., 42, 9512–9520,](#)  
848 [doi:10.1002/2015GL065497, 2015.](#)  
849

850 [Field, P. R., Lawson, R. P., Brown, P. R. A., Lloyd, G., Westbrook, C., Moisseev, D., Miltenberger, A., Nenes, A., Blyth, A.,](#)  
851 [Choulaton, T., Connolly, P., Buehl, J., Crosier, J., Cui, Z., Dearden, C., DeMott, P., Flossmann, A., Heymsfield, A., Huang,](#)  
852 [Y., Kalesse, H., Kanji, Z. A., Korolev, A., Kirchgaessner, A., Lasher-Trapp, S., Leisner, T., McFarquhar, G., Phillips, V.,](#)  
853 [Stith, J., and Sullivan, S.: Secondary Ice Production: Current State of the Science and Recommendations for the Future,](#)  
854 [Meteorological Monographs, 58, 7.1-7.20, doi: 10.1175/AMSMONOGRAPHIS-D-16-0014.1, 2017](#)

**Formatiert:** Links, Abstand Vor: 12 Pt., Nach: 12 Pt.,  
Zeilenabstand: Mehrere 1,15 ze

855

856 [Forster, P., Storelmo, T., Armour, K., Collins, W., Dufresne, J. L., Frame, D., Lunt, D. J., Mauritsen, T., Palmer, M. D.,](#)  
857 [Watanabe, M., Wild, M., and Zhang, H.: The Earth's Energy Budget, Climate Feedbacks, and Climate Sensitivity. In: \*Climate\*](#)  
858 [Change 2021: The Physical Science Basis. Contribution of Working Group I to the Sixth Assessment Report of the](#)  
859 [Intergovernmental Panel on Climate Change. Cambridge University Press, in press, 2021.](#)

860

861 [Frech, M., and Hubbert, J.: Monitoring the differential reflectivity and receiver calibration of the German polarimetric weather](#)  
862 [radar network, \*Atmos. Meas. Tech.\*, 13, 1051–1069, doi: 10.5194/amt-13-1051-2020, 2020.](#)

863

864 [Gao, W., Sui, C.-H., Chen Wang, T.-C. and Chang, W.-Y.: An evaluation and improvement of microphysical parameterization](#)  
865 [from a two-moment cloud microphysics scheme and the Southwest Monsoon Experiment \(SoWMEX\)/Terrain-influenced](#)  
866 [Monsoon Rainfall Experiment \(TiMREX\) observations, \*J. Geophys. Res. Atmos.\*, 116, 1-13, doi:10.1029/2011JD015718,](#)  
867 [2011.](#)

868

869 Gasper, F., Görgen, K., Shrestha, P., Sulis, M., Rihani, J., Geimer, M., and Kollet, S.: Implementation and scaling of the fully  
870 coupled Terrestrial Systems Modeling Platform (TerrSysMP v1. 0) in a massively parallel supercomputing environment—a  
871 case study on JUQUEEN (IBM Blue Gene/Q). [Geosci. Model Dev. Geoscientific model development](#), 7(5), 2531-2543, 2014.

872

873 [Gehring, J., Oertel, A., Vignon, E., Jullien, N., Besic, N., and Berne, A.: Microphysics and dynamics of snowfall associated](#)  
874 [with a warm conveyor belt over Korea, \*Atmos. Chem. Phys.\*, 20, 7373–7392, doi: 10.5194/acp-20-7373-2020, 2020.](#)

875

876 [Grazioli, J., Tuia, D., and Berne, A.: Hydrometeor classification from polarimetric radar measurements: a clustering approach,](#)  
877 [\*Atmos. Meas. Tech. Atmospheric Measurement Techniques\*, 8\(1\), pp.149-170, 2015.](#)

878

879 [Flamant, C., Knippertz, P., Fink, A.H., Akpo, A., Brooks, B., Chiu, C.J., Coe, H., Danuor, S., Evans, M., Jegede, O., Kalthoff,](#)  
880 [N., Konaré, A., Lioussé, C., Lohou, F., Mari, C., Schlager, H., Schwarzenboeck, A., Adler, B., Amekudzi, L., Aryee, J.,](#)  
881 [Ayoola, M., Batenburg, A.M., Bessardon, G., Borrmann, S., Brito, J., Bower, K., Burnet, F., Catoire, V., Colomb, A., Denjean,](#)  
882 [C., Fosu-Amankwah, K., Hill, P.G., Lee, J., Lothon, M., Maranan, M., Marsham, J., Meynadier, R., Ngamini, J., Rosenberg,](#)  
883 [P., Sauer, D., Smith, V., Stratmann, G., Taylor, J.W., Voigt, C., and Yoboué, V.: The Dynamics–Aerosol–Chemistry–Cloud](#)  
884 [Interactions in West Africa Field Campaign: Overview and Research Highlights, \*B. Am. Meteorol. Soc. Bull.–Amer. Meteor.\*](#)  
885 [Soc.](#), 99, 83–104, <https://doi.org/10.1175/BAMS-D-16-0256.1>, 2018

886

887 [Fridlind, A. M., van Lier-Walqui, M., Collis, S., Giangrande, S. E., Jackson, R. C., Li, X., Matsui, T., Orville, R., Picel, M.](#)  
888 [H., Rosenfeld, D., Ryzhkov, A., Weitz, R., and Zhang, P.: Use of polarimetric radar measurements to constrain simulated](#)  
889 [convective cell evolution: a pilot study with Lagrangian tracking, \*Atmos. Meas. Tech.\*, 12, 2979–3000, doi:10.5194/amt-12-](#)  
890 [2979-2019, 2019.](#)

891

892 Hashino, T., and Tripoli, G. J.: The Spectral Ice Habit Prediction System (SHIPS). Part I: Model Description and Simulation  
893 of the Vapor Deposition Process, [J. Atmos. Sci.](#) ~~Journal of the Atmospheric Sciences~~, 64(7), 2210-2237,  
894 doi:10.1175/JAS3963.1, 2007.

895

896 Heinze, R., Dipankar, A., Henken, C. C., Moseley, C., Sourdeval, O., Trömel, S., Xie, X., Adamidis, P., Ament, F., Baars, H.  
897 Barthlott, C., Behrendt, A., Blahak, U., Bley, S., Brdar, S., Brueck, M., Crewell, S., Deneke, H., Girolamo, P. D., Evaristo,  
898 R., Fischer, J., Frank, C., Friederichs, P., Göcke, T., Gorges, K., Hande, L., Hanke, M., Hansen, A., Hege, H.-C., Hoose, C.,  
899 Jahns, T., Kalthoff, N., Klocke, D., Kneifel, S., Knippertz, P., Kuhn, A., Laar, T., Macke, A., Maurer, V., Mayer, B., Meyer,  
900 C. I., Muppa, S. K., Neggers, R. A. J., Orlandi, E., Pantillon, F., Pospichal, B., Röber, N., Scheck, L., Seifert, A., Seifert, P.,  
901 Senf, F., Siligam, P., Simmer, C., Steinke, S., Stevens, B., Wapler, K., Weniger, M., Wulfmeyer, V., Zängl, G., Zhang, D.,  
902 and Quaas, J.: Large-eddy simulations over Germany using ICON: A comprehensive evaluation, [Q. J. Roy. Meteor. Soc. Quart-](#)  
903 [J. Roy. Meteorol. Soc.](#), 143, 69-100, doi:10.1002/qj.2947, 2017.

904

905 Heymsfield, A., Bansemer, A., Wood, N. B., Liu, G., Tanelli, S., Sy, O. O., Poellot, M., and Liu, C.: Toward Improving Ice  
906 Water Content and Snow-Rate Retrievals from Radars. Part II: Results from Three Wavelength Radar-Collocated In Situ  
907 Measurements and CloudSat-GPM-TRMM Radar Data, [J. Appl. Meteor. Climatol.](#) ~~Journal of Applied Meteorology and~~  
908 [Climatology](#), 57(2), 365-389. Retrieved Apr 6, 2021, from [https://journals.ametsoc.org/view/journals/apme/57/2/jamc-d-17-](https://journals.ametsoc.org/view/journals/apme/57/2/jamc-d-17-0164.1.xml)  
909 [0164.1.xml](#), 2018.

910

911 [Hogan, R. J., Tian, L., Brown, P. R. A., Westbrook, C. D., Heymsfield, A. J., and Eastment, J. D.: Radar Scattering from Ice](#)  
912 [Aggregates Using the Horizontally Aligned Oblate Spheroid Approximation, \*J. Appl. Meteor. Climatol.\* ~~Journal of Applied~~](#)  
913 [Meteorology and Climatology](#), 51(3), 655-671, doi:10.1175/JAMC-D-11-074.1, 2012.

914

915 Ilotoviz, E., Khain, A., Ryzhkov, A. V., and Snyder, J. C.: Relation between Aerosols, Hail Microphysics, and ZDR Columns,  
916 *J. Atmos. Sci.*, 75, 1755-1781, doi:10.1175/JAS-D-17-0127.1, 2018.

917

918 Janjic, T., Bormann, N., Bocquet, M., Carton, J. A., Cohn, S. E., Dance, S. L., Losa, S. N., Nichols, N. K., Potthast, R., Waller,  
919 J. A., and Weston, P.: On the representation error in data assimilation, *Q. J. R. Meteorol. Soc.*, 144:713, 1257-1278, 2018.

Formatiert: Schriftart: Nicht Kursiv

920  
921 Jung, Y., Xue, M., Zhang, G., and Straka, J.: Assimilation of simulated polarimetric radar data for a convective storm using  
922 ensemble Kalman filter. Part II: Impact of polarimetric data on storm analysis, *Mon. Wea. Rev.*, 136, 2246–2260,  
923 [doi:10.1175/2007MWR2288.1](https://doi.org/10.1175/2007MWR2288.1), 2008.

924  
925 Jung, Y., Xue, M., and Zhang, G.: Simultaneous Estimation of Microphysical Parameters and the Atmospheric State Using  
926 Simulated Polarimetric Radar Data and an Ensemble Kalman Filter in the Presence of an Observation Operator Error, *Mon.*  
927 *Wea. Rev.*, 138, 539–562, [doi:10.1175/2009MWR2748.1](https://doi.org/10.1175/2009MWR2748.1), 2010.

928  
929 [Jung, Y., Xue, M., and Tong, M.: Ensemble Kalman Filter Analyses of the 29–30 May 2004 Oklahoma Tornadoic  
930 Thunderstorm Using One- and Two-Moment Bulk Microphysics Schemes, with Verification against Polarimetric Radar Data,  
931 \*Mon. Wea. Rev.\*, 140, 1457-1475, \[doi: MWR-D-11-00032.1\]\(https://doi.org/MWR-D-11-00032.1\), 2012](#)

932  
933 [Kalesse, H., Szyrmer, W., Kneifel, S., Kollias, P., and Luke, E.: Fingerprints of a riming event on cloud radar Doppler spectra:  
934 observations and modeling, \*Atmos. Chem. Phys.\*, 16, 2997–3012, \[doi: 10.5194/acp-16-2997-2016\]\(https://doi.org/10.5194/acp-16-2997-2016\), 2016.](#)

935  
936 Khain, A., Rosenfeld, D., and Pokrovsky, A.: Aerosol impact on the dynamics and microphysics of convective clouds, *Q. J.*  
937 *R. Meteorol. Soc.*, 131, 2639–2663, [doi:10.1256/qj.04.62](https://doi.org/10.1256/qj.04.62), 2005.

938  
939 Khain, A. P., Beheng, K. D., Heymsfield, A., Korolev, A., Krichak, S. O., Levin, Z., Pinsky, M., Phillips, V., Prabhakaran, T.,  
940 Teller, A., et al.: Representation of microphysical processes in cloud-resolving models: Spectral (bin) microphysics versus  
941 bulk parameterization, *Rev. Geophys.*, 53, 247– 322, [doi:10.1002/2014RG000468](https://doi.org/10.1002/2014RG000468), 2015.

942  
943 Kleine, J., Voigt, C., Sauer, D., Schlager, H., Scheibe, M., Kaufmann, S. , Jurkat-Witschas, T., Kärcher, B., and Anderson B.:  
944 In situ observations of ice particle losses in a young persistent contrail, *Geophys. Res. Lett.*, [doi:10.1029/2018GL079390](https://doi.org/10.1029/2018GL079390), 2018.

945  
946 Kneifel S., A. von Lerber, J. Tiira, D. Moisseev, P. Kollias, and J. Leinonen: Observed Relations between Snowfall  
947 Microphysics and Triple-frequency Radar Measurements, *J. Geophys. Res.*, 120, 6034-6055, [doi: 10.1002/2015JD023156](https://doi.org/10.1002/2015JD023156),  
948 2015.

949  
950 [Kneifel, S., and Moisseev, D.: Long-term statistics of riming in non-convective clouds derived from ground-based Doppler  
951 cloud radar observations, \*J. Atmos. Sci.\*, 77, 3495–3508, \[doi: 10.1175/JAS-D-20-0007.1\]\(https://doi.org/10.1175/JAS-D-20-0007.1\), 2020.](#)

952

953 [Kollias, P., Albrecht, B.A., and Marks Jr F.: Why Mie? Accurate observations of vertical air velocities and raindrops using a](#)  
954 [cloud radar. Bulletin of the American Meteorological Society, 83\(10\), 1471-1484, doi: 10.1175/BAMS-83-10-1471 2002](#)  
955

956 [Kumjian, M.R.: Principles and applications of dual-polarization weather radar. Part I: Description of the polarimetric radar](#)  
957 [variables. J. Operational Meteor., 1\(19\), 226-242, doi: 10.15191/nwajom.2013.0119, 2013](#)  
958

959 [Kumjian, M. R.: The impact of precipitation physical processes on the polarimetric radar variables, Dissertation, University](#)  
960 [of Oklahoma, Norman Campus, https://hdl.handle.net/11244/319188, 2012](#)  
961

962 [Kumjian, M. R., Khain, A. P., Benmoshe, N., Ilotoviz, E., Ryzhkov, A. V., and Phillips, V. T. J.: The anatomy and physics of](#)  
963 [Z<sub>DR</sub> columns: Investigating a polarimetric radar signature with a spectral bin microphysical model, J. Appl. Meteor.](#)  
964 [Climatol. Journal of Applied Meteorology and Climatology, 53, 1820-1843, 2014.](#)  
965

966 [Kumjian, M. R., Tobin, D. M., Oue, M., and Kollias, P.: Microphysical insights into ice pellet formation revealed by fully](#)  
967 [polarimetric Ka-band Doppler radar, J. Appl. Meteor. Climatol., 59, 1557–1580, doi: 10.1175/JAMC-D-20-0054.1, 2020.](#)  
968

969 [Kuster, C. M., Schuur, T. J., Lindley, T. T., and Snyder, J. C.: Using ZDR Columns in Forecaster Conceptual Models and](#)  
970 [Warning Decision-Making, Weather and Forecasting, 35\(6\), 2507-2522, 2020.](#)  
971

972 [Le Treut, H. and Li, Z.-X.: Sensitivity of an atmospheric general circulation model to prescribed SST changes: Feedback](#)  
973 [effects associated with the simulation of cloud optical properties, Clim. Dyn., 5, 175–187, 1991.](#)  
974

975 [Li, H., and Moisseev, D.: Two layers of melting ice particles within a single radar bright band: interpretation and implications,](#)  
976 [Geophys. Res. Lett., 47, e2020GL087499, doi: 10.1029/2020GL087499, 2020.](#)  
977

978 [Libbrecht, K. G.: The physics of snow crystals, Rep. Prog. Phys., 68, 855–895, doi:10.1088/0034-4885/68/4/R03, 2005.](#)  
979

980 [Lohmann U. und E. Roeckner, Design and performance of a new cloud microphysics scheme developed for the ECHAM](#)  
981 [general circulation model, Clim. Dyn., 12, 557-572, 1996.](#)  
982

983 [Lukach, M., Dufton, D., Crosier, J., Hampton, J.M., Bennett, L. and Neely III, R.R. Hydrometeor classification of quasi-](#)  
984 [vertical profiles of polarimetric radar measurements using a top-down iterative hierarchical clustering method. \*Atmos. Meas.\*](#)  
985 [Tech, 14\(2\), pp.1075-1098, 2021](#)

986  
987 [Luke E.P., Yang, F., Kollias, P., Vogelmann, A.M., Maahn, M.: New insights into ice multiplication using remote-sensing](#)  
988 [observations of slightly supercooled mixed-phase clouds in the Arctic. \*PNAS\*, 118\(13\), e2021387118,](#)  
989 [doi:10.1073/pnas.2021387118, 2021](#)

990 [Matrosov, S. Y., Reinking, R. F., Kropfli, R. A., Martner, B. E., and Bartram, B. W. \(2001\). On the use of radar depolarization](#)  
991 [ratios for estimating shapes of ice hydrometeors in winter clouds, \*Journal of Applied Meteorology\*, 40, 479-490,](#)  
992 [doi:10.1175/1520-0450\(2001\)040h0479:OTUORDi2.0.CO;2.](#)

993  
994 Matsui, T., Dolan, B., Rutledge, S. A., Tao, W.-K., Iguchi, T., Barnum, J., and Lang, S. E.: POLARRIS: A POLARimetric  
995 Radar Retrieval and Instrument Simulator, [J. Geophys. Res.-Atmos.](#)~~Journal of Geophysical Research: Atmospheres~~, 124,  
996 4634–4657, doi:10.1029/2018JD028317, 2019.

997  
998 Mellado, J.P., Stevens, B., Schmidt, H., and Peters, N.: Buoyancy reversal in cloud-top mixing layers, *Q.J.R. Meteorol. Soc.*,  
999 135: 963-978., doi:10.1002/qj.417, 2009.

1000  
1001 Mendrok, J., Blahak, U., Snyder, J. C., and Carlin, J. T.: The polarimetric efficient modular volume scan radar forward operator  
1002 Pol-EMVORADO, *Geosci. Model Dev.*, 2021 (in preparation for this Special Issue).

1003  
1004 Mishchenko, M. I.: Calculation of the amplitude matrix for a nonspherical particle in a fixed orientation, *Appl. Opt.* 39, 1026-  
1005 1031, ~~2000~~.

1006  
1007 Moisseev, D. N., Lautaportti, S., Tyynela, J., and Lim, S.: Dualpolarization radar signatures in snowstorms: Role of snowflake  
1008 aggregation, *J. Geophys. Res. Atmos.*, 120, 12 644–12 655, doi:10.1002/2015JD023884, 2015.

1009  
1010 Morrison, H. and Milbrandt, J. A.: Parameterization of Cloud Microphysics Based on the Prediction of Bulk Ice Particle  
1011 Properties. Part I: Scheme Description and Idealized Tests, [J. Atmos. Sci.](#)~~Journal of the Atmospheric Sciences~~, 72(1), 287-  
1012 311, 2015.

1014 [Morrison, H., van Liefer-Walqui, M., Fridlind, A. M., Grabowski, W. W., Harrington, J. Y., and Hoose, C., et al.: Confronting](#)  
1015 [the challenge of modeling cloud and precipitation microphysics. \*Journal of Advances in Modeling Earth Systems\*, 12,](#)  
1016 [e2019MS001689. doi:10.1029/2019MS001689, 2020.](#)

1017  
1018 Mülmenstädt, J., Sourdeval, O., Delanoë, J., and Quaas, J.: Frequency of occurrence of rain from liquid-, mixed- and ice-phase  
1019 clouds derived from A-Train satellite retrievals, *Geophys. Res. Lett.*, 42, 6502-6509, doi:10.1002/2015GL064604, 2015.

1020 [Murphy, A. M., Ryzhkov, A., & Zhang, P.: Columnar vertical profile \(CVP\) methodology for validating polarimetric radar](#)  
1021 [retrievals in ice using in situ aircraft measurements. \*J. Atmos. Oceanic Technol.\*, 37\(9\), 1623-1642, doi:10.1175/JTECH-D-](#)  
1022 [20-0011.1, 2020.](#)

1023  
1024 Myagkov, A., Seifert, P., Bauer-Pfundstein, M., and Wandinger, U.: Cloud radar with hybrid mode towards estimation of  
1025 shape and orientation of ice crystals, *Atmos. Meas. Tech.*, 9, 469–489, doi:10.5194/amt-9-469-2016, 2016.

1026  
1027 Neggers, R. A.: A dual mass flux framework for boundary layer convection. Part II: Clouds, *J. Atmos. Sci.*, 66, 1489–1506,  
1028 doi:10.1175/2008JAS2636.1, 2009.

1029  
1030 Neto, J. D., Kneifel, S., Ori, D., Trömel, S., Handwerker, J., Bohn, B., Hermes, N., Mühlbauer, K., Lenefer, M., and Simmer,  
1031 C.: The TRIPLE-frequency and Polarimetric radar Experiment for improving process observation of winter precipitation. *Earth*  
1032 *Syst. Sci. Data*, 11, 845–863, doi: 10.5194/essd-11-845-2019, 2019.

1033  
1034 Nguyen, C., Wolde, M., Baibakov, K., and Korolev, A.: Detection and estimation of high ice water content using X- and W-  
1035 band dual-polarization airborne radar data, 38th Conf. on Radar Meteorology, Chicago, IL, Amer. Meteor. Soc., 89,  
1036 <https://ams.confex.com/ams/38RADAR/webprogram/Paper321101.html>, 2017.

1037  
1038 Nguyen, C. M., Wolde, M., and Korolev, A.: Determination of ice water content (IWC) in tropical convective clouds from X-  
1039 band dual-polarization airborne radar. *Atmos. Meas. Tech.*, 12, 5897–5911, doi: 10.5194/amt-12-5897-2019, 2019.

1040  
1041 Ori, D., V. Schemann, M. Karrer, J. Dias Neto, L. von Terzi, A. Seifert, and S. Kneifel: Evaluation of ice particle growth in  
1042 ICON using statistics of multi-frequency Doppler cloud radar observations, *Q. J. Roy. Meteor. Soc.*, 146: 3830– 3849.  
1043 [https://doi.org/10.1002/qj.3875\\_2020](https://doi.org/10.1002/qj.3875_2020)



1044 [Oue, M., A. Tatarevic, P. Kollias, D. Wang, K. Yu, and A.M. Vogelmann: The Cloud-resolving model Radar SIMulator \(CR-](#)  
1045 [SIM\) Version 3.3: description and applications of a~virtual observatory, \*Geoscientific Model Development\*, 13: 1975-1998,](#)  
1046 [doi: 10.5194/gmd-13-1975-2020, 2020.](#)

1047 [Oue, M., Kollias, P., Ryzhkov, A., and Luke, E. P.: Toward exploring the synergy between cloud radar polarimetry and Doppler](#)  
1048 [spectral analysis in deep cold precipitating systems in the Arctic, \*J. Geophys. Res. Atmos.\*, 123, 2797-2815, doi:](#)  
1049 [10.1002/2017JD027717, 2018.](#)

1050 Phillips, V. T. J., Yano, J., & Khain, A. (2017). Ice Multiplication by Breakup in Ice-Ice Collisions. Part I: Theoretical  
1051 Formulation, *J. Atmos. Sci.*, 74(6), 1705-1719

1052 [Pfitzenmayer L., Unal, C. M. H., Dufournet, Y., Ruschenberg, H. W. J.: Observing ice particle growth along fall streaks in](#)  
1053 [mixed-phase clouds using spectral polarimetric radar data, \*Atmos. Chem. Phys.\*, 18, 7843-7863, doi: 10.5194/acp-18-7843-](#)  
1054 [2018, 2018.](#)

1055 Pincus, R. and Klein, S.: Unresolved spatial variability and microphysical process rates in large-scale models, *J. Geophys.*  
1056 *Res.*, 105, 27059 - 27065, 2000.

1057

1058 Putnam, B., Xue, M., Jung, Y., Snook, N., and Zhang, G.: Ensemble Kalman Filter Assimilation of Polarimetric Radar  
1059 Observations for the 20 May 2013 Oklahoma Tornadoic Supercell Case, *Mon. Wea. Rev.*, 147, 2511-2533, [doi:10.1175/MWR-](#)  
1060 [D-18-0251.1](#), 2019.

1061

1062 [Radenz, M., Bühl, J., Seifert, P., Baars, H., Engelmann, R., Barja González, B., Mamouri, R.-E., Zamorano, F., and Ansmann,](#)  
1063 [A.: Hemispheric contrasts in ice formation in stratiform mixed-phase clouds: Disentangling the role of aerosol and dynamics](#)  
1064 [with ground-based remote sensing, \*Atmos. Chem. Phys. Discuss.\* \[preprint\], <https://doi.org/10.5194/acp-2021-360>, in review,](#)  
1065 [2021.](#)

1066

1067 Reimann, L., Simmer, C., and Trömel, S.: Dual-polarimetric radar estimators of liquid water content over Germany,- Accepted  
1068 for *Meteorol. Z. (Contrib. Atm. Sci.)*, doi:[10.1127/metz/2021/1072](#), 2021.

1069

1070 [Ribaud, J.-F., L. A. T. Machado, and T. Biscaro: X-band dual-polarization radar-based hydrometeor classification for Brazilian](#)  
1071 [tropical precipitation systems, \*Atmos. Meas. Tech.\*, 12, 811-837, doi.org/10.5194/amt-12-811-2019, 2019.](#)

1072

1073 Rosch, J., et al.: Analysis of diagnostic climate model cloud parameterisations using large-eddy simulations, *Q. J. R. Meteorol.*  
1074 *Soc.*, 141, 2199-2205, doi:[10.1002/qj.2515](#), 2015.

- 1075  
1076 Rotstayn, L. D.: On the tuning of autoconversion parameterizations in climate models, *J. Geophys. Res.*, 105, 15,495–15,507,  
1077 2000.
- 1078  
1079 Ryzhkov, A. V., Zrníc, D. S., and Gordon, B. A.: Polarimetric Method for Ice Water Content Determination, *J. Appl. Meteor.*  
1080 *Climatol., Journal of Applied Meteorology* 37, 125-134, 1998.
- 1081  
1082 Ryzhkov, A., Pinsky, M., Pokrovsky, A., and Khain, A.: Polarimetric Radar Observation Operator for a Cloud Model with  
1083 Spectral Microphysics, *J. Appl. Meteor. Climatol.*, 50, 873-894, 2011.
- 1084  
1085 Ryzhkov, A., Zhang, P., Reeves, H., Kumjian, M., Tschallener, T., Trömel, S., and Simmer, C.: Quasi-vertical profiles – a  
1086 new way to look at polarimetric radar data, *J. Atmos. Oceanic Technol.*, 33, 551-562, [doi: 10.1175/JTECH-D-15-0020.1](https://doi.org/10.1175/JTECH-D-15-0020.1), 2016.
- 1087  
1088 Ryzhkov, A., Bukovcic, P., Murphy, A., Zhang, P., and McFarquhar, G.: Ice Microphysical Retrievals Using Polarimetric  
1089 Radar Data. In Proceedings of the 10th European Conference on Radar in Meteorology and Hydrology, Ede, The Netherlands,  
1090 1–6 July 2018.
- 1091  
1092 Ryzhkov, A. and Zrníc, D.: *Radar Polarimetry for Weather Observations*, Springer Atmospheric Sciences, 486 pp., 2019.
- 1093  
1094 Schinagl, K., Friederichs, P., Trömel, S., and Simmer, C.: Gamma Drop Size Distribution Assumptions in Bulk Model  
1095 Parameterizations and Radar Polarimetry and Their Impact on Polarimetric Radar Moments, *J. Appl. Meteor. Climatol.*, 58,  
1096 467–478, [doi: 10.1175/JAMC-D-18-0178.1](https://doi.org/10.1175/JAMC-D-18-0178.1), 2019.
- 1097  
1098 Schrom, R. S. and Kumjian, M. R.: Bulk-Density Representations of Branched Planar Ice Crystals: Errors in the Polarimetric  
1099 Radar Variables, *J. Appl. Meteor. Climatol., Journal of Applied Meteorology and Climatology*, 57(2), 333-346, 2018.
- 1100  
1101 Seifert, A. and Beheng, K. D.: A two-moment cloud microphysics parameterization for mixed-phase clouds. Part 1: Model  
1102 description, *Meteorol. Atmos. Phys.*, 92, 45-66, [doi: 10.1007/s00703-005-0112-4](https://doi.org/10.1007/s00703-005-0112-4), 2006.
- 1103  
1104 Shrestha, P., Sulis, M., Masbou, M., Kollet, S. and Simmer, C: A scale-consistent Terrestrial System Modeling Platform based  
on COSMO, CLM and ParFlow, *Mon. Wea. Rev.*, 142, 3466-3483, [doi: 10.1175/MWR-D-14-00029.1](https://doi.org/10.1175/MWR-D-14-00029.1), 2014
- 1105  
1106 Shrestha, P.: Clouds and vegetation modulate shallow groundwater table depth, 22, 753 – 763, <https://doi.org/10.1175/JHM-D-20-0171.1>, 2021

1107 [Shrestha, P., Trömel, S., Evaristo, R., and Simmer, C.: Evaluation of modeled summertime convective storms using](#)  
1108 [polarimetric radar observations, \*Atmos. Chem. Phys. Discuss.\* \[preprint\], <https://doi.org/10.5194/acp-2021-404>, in review,](#)  
1109 [2021a.](#)

1110 Shrestha, P., Mendrok, J., Pejic, V., Trömel, S., and Blahak, U.: The impact of uncertainties in model microphysics, retrievals  
1111 and forward operators on model evaluations in polarimetric radar space, [Geosci. Model Dev. Geoscientific Model](#)  
1112 [Development](#), 2021b (submitted).

1113  
1114 [Shupe, M. D., Kollias, P., Matrosov, S. Y., and Schneider, T. L.: Deriving mixed-phase cloud properties from Doppler radar](#)  
1115 [spectra, \*J. Atmos. Oceanic Technol.\*, 21, 660–670, doi: 10.1175/1520-0426\(2004\)021<0660:DMCPFD>2.0.CO;2, 2004.](#)

1116  
1117 Simmel, M., Bühl, J., Ansmann, A., and Tegen, I.: Ice phase in altocumulus clouds over Leipzig: remote sensing observations  
1118 and detailed modeling, *Atmos. Chem. Phys.*, 15, 10453–10470, doi:10.5194/acp-15-10453-2015, 2015.

1119  
1120 Simmer, C., Thiele-Eich, I., Masbou, M., Amelung, W., Crewell, S., Diekkrueger, B., Ewert, F., Hendricks Franssen, H.-J.,  
1121 Huisman, A. J., Kemna, A., Klitzsch, N., Kollet, S., Langensiepen, M., Löhnert, U., Rahman, M., Rascher, U., Schneider, K.,  
1122 Schween, J., Shao, Y., Shrestha, P., Stiebler, M., Sulis, M., Vanderborcht, J., Vereecken, H., van der Kruk, J., Zerenner, T.,  
1123 and Waldhoff, G.: Monitoring and Modeling the Terrestrial System from Pores to Catchments - the Transregional  
1124 Collaborative Research Center on Patterns in the Soil-Vegetation-Atmosphere System, [B. Am. Meteorol. Soc. Bulletin of the](#)  
1125 [American Meteorological Society](#), 96, 1765–1787, doi: <http://dx.doi.org/10.1175/BAMS-D-13-00134.1>, 2015.

1126  
1127 Simmer, C., Adrian, G., Jones, S., Wirth, V., Goeber, M., Hohenegger, C., Janjic, T., Keller, J., Ohlwein, C., Seifert, A.,  
1128 Trömel, S., Ulbrich, T., Wapler, K., Weissmann, M., Keller, J., Masbou, M., Meilinger, S., Riss, N., Schomburg, A., Vormann,  
1129 A., and Weingaertner, C.: HErZ - The German Hans-Ertel Centre for Weather Research. [B. Am. Meteorol. Soc. Bulletin of the](#)  
1130 [American Meteorological Society](#), p.1057-1068, doiDOI: <http://dx.doi.org/10.1175/BAMS-D-13-00227.1>, 2014

1131  
1132 Smith, R. N.: A scheme for predicting layer clouds and their water content in a general circulation model, *Q. J. R. Meteorol.*  
1133 *Soc.*, 116, 435–460, doi:10.1002/qj.49711649210, 1990.

1134  
1135 Snyder, J.C., Ryzhkov, A.V., Kumjian, M.R., Khain, A.P., and Picca, J.C.: A ZDR column detection algorithm to examine  
1136 convective storm updrafts, *Weather and Forecasting*, 30, 1819-1844, 2015.

1137  
1138 Sommeria, G. and Deardorff, J. W.: Subgrid-scale condensation models of non-precipitating clouds, *J. Atmos. Sci.*, 34, 344-  
1139 355, 1977.

1141 Sourdeval, O., Gryspeerdt, E., Krämer, M., Goren, T., Delanoë, J., Afchine, A., Hemmer, F., and Quaas, J.: Ice crystal number  
1142 concentration estimates from lidar–radar satellite remote sensing – Part 1: Method and evaluation, *Atmos. Chem. Phys.*, 18,  
1143 14327–14350, doi: [10.5194/acp-18-14327-2018](https://doi.org/10.5194/acp-18-14327-2018), 2018.

1144  
1145 Spek, A. L. J., Unal, C. M. H., Moisseev, C. N., Russchenberg, H. W. J., Chandrasekar, V., Dufournet, Y.: A New Techniques  
1146 to Categorize and Retrieve the Microphysical Properties of Ice Particles above the Melting Layer Using Radar Dual-  
1147 Polarization Spectral Analysis, *Jtech*, doi: 10.1175/2007JTECHA944.1, 2008.

1148  
1149 Stevens, B., Acquistapace, C., Hansen, A., Heinze, R., Klinger, C., Klocke, D., Schubotz, W., Windmiller, J., Adamidis, P.,  
1150 Arka, I., Barlakas, V., Biercamp, J., Brueck, M., Brune, S., Buehler, S., Burkhardt, U., Cioni, G., Costa-Surós, M., Crewell,  
1151 S., Crueger, T., Deneke, H., Friederichs, P., Carbajal Henken, C., Hohenegger, C., Jacob, M., Jakub, F., Kalthoff, N., Köhler,  
1152 M., Van Laar, T. W., Li, P., Löhnert, U., Macke, A., Madenach, N., Mayer, B., Nam, C., Naumann, A. K., Peters, K., Poll, S.  
1153 , Quaas, J., Röber, N., Rochetin, N., Rybka, H., Scheck, L., Schemann, V., Schnitt, S., Seifert, A., Senf, F., Shapkalijevski,  
1154 M., Simmer, C., Singh, S., Sourdeval, O., Spickermann, D., Strandgren, J., Tessiot, O., Vercauteren, N., Vial, J., Voigt, A.,  
1155 and Zängl, G.: Large-eddy and storm resolving models for climate prediction - the added value for clouds and precipitation, *J.*  
1156 *Meteorol. Soc. Japan*, 98, doi:10.2151/jmsj.2020-021, 2020.

1157  
1158 Stevens, B., et al.: Atmospheric component of the MPI-M Earth System Model: ECHAM6, *J. Adv. Model. Earth Syst.* 5: 146–  
1159 172, doi: 10.1002/jame.20015, 2013.

1160  
1161 Stevens, B. and Feingold, G.: Untangling Aerosol Effects on Clouds and Precipitation in a Buffered System, *Nature*, 461, 607–  
1162 613, 2009.

1163  
1164 Sundqvist, H., et al., Condensation and cloud parameterization studies with a mesoscale numerical weather prediction model,  
1165 *Mon. Weather Rev.*, 117, 1641–1657, 1989.

1166  
1167 Takahashi, T.: High ice crystal production in winter cumuli over the Japan Sea, *Geophysical research letters*, 20,6, 451–454,  
1168 1993.

1169  
1170 Takahashi, T., Yoshihiro N., and Yuzuru K.: Possible high ice particle production during graupel–graupel collisions, *J. Atmos.*  
1171 *Sci. Journal of the atmospheric sciences*, 52,24, 4523–4527, 1995.

1172  
1173 Takahashi, T.: Influence of liquid water content and temperature on the form and growth of branched planar snow crystals in  
1174 a cloud, *J. Atmos. Sci. Journal of the Atmospheric Sciences*, 71,11, 4127–4142, 2014.

1175  
1176 Tiedtke, M.: Representation of clouds in large scale models, *Mon. Weather Rev.*, 121, 3040–3061, 1993.  
1177  
1178 Tompkins, A.: A prognostic parameterization for the subgrid-scale variability of water vapor and clouds in large-scale models  
1179 and its use to diagnose cloud cover, *J. Atmos. Sci.*, 59:1917- 1942, 2002.  
1180  
1181 Trömel, S., Quaas, J., Crewell, S., Bott, A., and Simmer, C.: Polarimetric Radar Observations Meet Atmospheric Modelling.  
1182 19th International Radar Symposium (IRS), Bonn, doi: 10.23919/IRS.2018.8448121, 2018.  
1183  
1184 Trömel, S., Ryzhkov, A. V., Hickman, B., Mühlbauer, K., and Simmer, C.: Polarimetric Radar Variables in the Layers of  
1185 Melting and Dendritic Growth at X Band—Implications for a Nowcasting Strategy in Stratiform Rain, *J. Appl. Meteor.*  
1186 *Climatol.*, 58, 2497–2522, <https://doi.org/10.1175/JAMC-D-19-0056.1>, 2019.  
1187  
1188 Trömel, S., A. V. Ryzhkov, P. Zhang, and C. Simmer: The microphysical information of backscatter differential phase  $\delta$  in the  
1189 melting layer, *J. Appl. Meteor. Climatol. Journal of Applied Meteorology and Climatology*, 53, 2344-2359, 2014.  
1190  
1191 [Verlinde, J., Rambukkange, M. P., Clothiaux, E. E., McFarquhar, G. M., and Eloranta, E. W.: Arctic multilayered, mixed-](#)  
1192 [phase cloud processes revealed in millimeter-wave cloud radar Doppler spectra, \*J. Geophys. Res. Atmos.\*, 118, 13199–13213,](#)  
1193 [doi: 10.1002/2013JD020183, 2013.](#)  
1194  
1195 [Vogl, T., Maahn, M., Kneifel, S., Schimmel, W., Moisseev, D., and Kalesse-Los, H.: Using artificial neural networks to predict](#)  
1196 [riming from Doppler cloud radar observations, \*Atmos. Meas. Tech. Discuss.\* \[preprint\], <https://doi.org/10.5194/amt-2021-137>,](#)  
1197 [in review, 2021.](#)  
1198  
1199 Voigt, C., Schumann, U., Jurkat, T., Schäuble, D., Schlager, H., Petzold, A., Gayet, J.-F., Krämer, M., Schneider, J., Borrmann,  
1200 S., Schmale, J., Jessberger, P., Hamburger, T., Lichtenstern, M., Scheibe, M., Gourbeyre, C., Meyer, J., Kübbeler, M., Frey,  
1201 W., Kalesse, H., Butler, T., Lawrence, M. G., Holzäpfel, F., Arnold, F., Wendisch, M., Döpelheuer, A., Gottschaldt, K.,  
1202 Baumann, R., Zöger, M., Sölch, I., Rautenhaus, M., and Dörnbrack, A.: In-situ observations of young contrails – overview  
1203 and selected results from the CONCERT campaign, *Atmos. Chem. Phys.*, 10, 9039–9056, [https://doi.org/10.5194/acp-10-](https://doi.org/10.5194/acp-10-9039-2010)  
1204 [9039-2010](#), 2010.  
1205  
1206 Voigt, C., Jeßberger, P., Jurkat, T., Kaufmann, S., Baumann, R., Schlager, H., Bobrowski, N., Guffirda, G., and Salerno, G.:  
1207 Evolution of CO<sub>2</sub>, SO<sub>2</sub>, HCl and HNO<sub>3</sub> in the volcanic plumes from Etna, *Geophys. Res. Lett.*, 41,  
1208 doi:10.1002/2013GL058974, 2014.

1209

1210 Voigt, C., Schumann, U., Minikin, A., Abdelmonem, A., Afchine, A., Borrmann, S., Boettcher, M., Buchholz, B., Bugliaro,  
1211 L., Costa, A., Curtius, J., Dollner, M., Dörnbrack, A., Dreiling, V., Ebert, V., Ehrlich, A., Fix, A., Forster, L., Frank, F.,  
1212 Fütterer, D., Giez, A., Graf, K., Grooß, J., Groß, S., Heimerl, K., Heinold, B., Hüneke, T., Järvinen, E., Jurkat, T., Kaufmann,  
1213 S., Kenntner, M., Klingebiel, M., Klimach, T., Kohl, R., Krämer, M., Krisna, T. C., Luebke, A., Mayer, B., Mertes, S.,  
1214 Molleker, S., Petzold, A., Pfeilsticker, K., Port, M., Rapp, M., Reutter, P., Rolf, C., Rose, D., Sauer, D., Schäfler, A., Schlage,  
1215 R., Schnaiter, M., Schneider, J., Spelten, N., Spichtinger, P., Stock, P., Walser, A., Weigel, R., Weinzierl, B., Wendisch, M.,  
1216 Werner, F., Wernli, H., Wirth, M., Zahn, A., Ziereis, H., and Zöger, M.; ML-CIRRUS: The Airborne Experiment on Natural  
1217 Cirrus and Contrail Cirrus with the High-Altitude Long-Range Research Aircraft HALO, *B. Am. Meteorol. Soc. Bulletin of*  
1218 *the American Meteorological Society*, 98(2), 271-288, doi:[bams-d-15-00213.1](https://doi.org/10.1175/BAMS-D-15-00213.1), 2017.

Formatiert: Schriftart: Nicht Kursiv

Formatiert: Schriftart: Nicht Kursiv

1219 Voigt, C., Lelieveld, J., Schlager, H., Schneider, J., Sauer, D., Meerkötter, R., Pöhlker, M., Bugliaro, L., Curtius, J.,  
1220 Erbertseder, T., Hahn, V., Jöckel, P., Li, Q., Marsing, A., Mertens, M., Pöhlker, C., Pöschl, U., Pozzer, A., Tomsche, L., and  
1221 Schumann, U.: Aerosol and Cloud Changes during the Corona Lockdown in 2020 - First highlights from the BLUESKY  
1222 campaign; EGU21-13134, <https://meetingorganizer.copernicus.org/EGU21/session/40818>, 2021.

1223 [Wang, M., Zhao, K., Pan, Y., Xue, M.: Evaluation of simulated drop size distributions and microphysical processes using](#)  
1224 [polarimetric radar observations for landfalling Typhoon Matmo \(2014\), J. Geophys. Res. Atmos., 125, 1-20,](#)  
1225 [doi:10.1029/2019JD031527, 2020.](#)

1226 Weissmann, M., M. Göber, C. Hohenegger, T. Janjic, J. Keller, C. Ohlwein, A. Seifert, S. Trömel, T. Ulbrich, K. Wapler, C.  
1227 Bollmeyer, H. Deneke: The Hans-Ertel Centre for Weather Research – Research objectives and highlights from its first three  
1228 years. *Meteorol. Z.*, 23(3), 193 – 208, 2014.

1229 Wendisch, M., Pöschl, U., Andreae, M. O., Machado, L. A. T., Albrecht, R., Schlager, H., Rosenfeld, D., Martin, S. T.,  
1230 Abdelmonem, A., Afchine, A., Araújo, A. C., Artaxo, P., Aufmhoff, H., Barbosa, H. M. J., Borrmann, S., Braga, R., Buchholz,  
1231 B., Cecchini, M. A., Costa, A., Curtius, J., Dollner, M., Dorf, M., Dreiling, V., Ebert, V., Ehrlich, A., Ewald, F., Fisch, G.,  
1232 Fix, A., Frank, F., Fütterer, D., Heckl, C., Heidelberg, F., Hüneke, T., Jäkel, E., Järvinen, E., Jurkat, T., Kanter, S., Kästner,  
1233 U., Kenntner, M., Kesselmeier, J., Klimach, T., Knecht, M., Kohl, R., Kölling, T., Krämer, M., Krüger, M., Krisna, T. C.,  
1234 Lavric, J. V., Longo, K., Mahnke, C., Manzi, A. O., Mayer, B., Mertes, S., Minikin, A., Molleker, S., Münch, S., Nillius, B.,  
1235 Pfeilsticker, K., Pöhlker, C., Roiger, A., Rose, D., Rosenow, D., Sauer, D., Schnaiter, M., Schneider, J., Schulz, C., de Souza,  
1236 R. A. F., Spanu, A., Stock, P., Vila, D., Voigt, C., Walser, A., Walter, D., Weigel, R., Weinzierl, B., Werner, F., Yamasoe, M.  
1237 A., Ziereis, H., Zinner, T., and Zöger, M.: ACRIDICON–CHUVA Campaign: Studying Tropical Deep Convective Clouds and  
1238 Precipitation over Amazonia Using the New German Research Aircraft HALO, *B. Am. Meteorol. Soc. Bulletin of the American*  
1239 *Meteorological Society*, 97(10), 1885-1908, doi:[bams-d-14-00255.1](https://doi.org/10.1175/BAMS-D-14-00255.1), 2016.

Formatiert: Schriftart: Nicht Kursiv

1240 Wolfensberger, D. and Berne, A.: From model to radar variables: a new forward polarimetric radar operator for COSMO,  
1241 Atmos. Meas. Tech., 11, 3883-3916, doi: 10.5194/amt-11-3883-2018, 2018.

1242 Xie, X., Evaristo, R., Trömel, S., Saavedra, P., Simmer, C., and Ryzhkov, A.: Radar Observation of Evaporation and  
1243 Implications for Quantitative Precipitation and Cooling Rate Estimation, J. Atmos. Oceanic Technol. 33(8), 1779-1792,  
1244 doi:10.1175/JTECH-D-15-0244.1, 2016.

1245  
1246 Xie, X., Shrestha, P., Mendrok, J., Carlin, J., Trömel, S., and Blahak, U.: Bonn Polarimetric Radar forward Operator (B-PRO),  
1247 CRC/TR32 Database (TR32DB), doi:10.5880/TR32DB.41, 2021, (accessed 8 April 2021).

1248  
1249 [Xue, L., Fan, J., Lebo, Z. J., Wu, W., Morrison, H., Grabowski, W. W., Chu, X., Geresdi, I., North, K., Stenz, R., Gao, Y.,](#)  
1250 [Lou, X., Bansemer, A., Heymsfield, A. J., McFarquhar, G. M., and Rasmussen, R. M.: Idealized Simulations of a Squall Line](#)  
1251 [from the MC3E Field Campaign Applying Three Bin Microphysics Schemes: Dynamic and Thermodynamic Structure,](#)  
1252 [Monthly Weather Review, 145\(12\), 4789-4812, doi:10.1175/MWR-D-16-0385.1, 2017.](#)

1253  
1254 [You, C.-R., Chung, K.-S., and Tsai, C.-C.: Evaluating the performance of convection-permitting model by using dual-](#)  
1255 [polarimetric radar parameters: Case study of SoWMEX IOP8, Remote Sensing, 12\(18\):3004, 1-25, doi:10.3390/rs12183004,](#)  
1256 [2020.](#)

1257  
1258 Zängl, G., et al.: The ICON (icosahedral non-hydrostatic) modelling framework of DWD and MPI-M: Description of the non-  
1259 hydrostatic dynamical core, [Q. J. Roy. Meteor. Soc. Quart. J. Roy. Meteorol. Soc.](#), 141, 563–579, 2015.

1260  
1261 Zeng, Y., Janjic, T., Lozar, A. de, Welzbacher, C. A., Blahak, U., and Seifert, A.: Assimilating radar radial wind and reflectivity  
1262 data in an idealized setup of the COSMO-KENDA system, Atmospheric Research, 249, 105282,  
1263 doi:10.1016/j.atmosres.2020.105282, 2021a.

1264  
1265 [Zeng, Y., Janjic, T., Feng, Y., Blahak, U., de Lozar, A., Bauernschubert, E., Stephan, K., and Min, J.: Interpreting estimated](#)  
1266 [observation error statistics of weather radar measurements using the ICON-LAM-KENDA system, Atmos. Meas. Tech., 14,](#)  
1267 [5735–5756, https://doi.org/10.5194/amt-14-5735-2021, 2021b.](#)

1268  
1269 Zeng, Y., Janjic, T., Lozar, A. de, Rasp, S., Blahak, U., Seifert, A., and Craig, G. C.: Comparison of methods accounting for  
1270 subgrid-scale model error in convective-scale data assimilation, Mon. Wea. Rev., 148, 2457-2477, 2020.

1271

Formatiert: Schriftart: 8 Pt.

- 1272 Zeng Y., Janjic, T., Sommer, M., Lozar, A. de, Blahak, U., and Seifert, A.: Representation of model error in convective-scale  
1273 data assimilation: additive noise based on model truncation error, [J. Adv. Model. Earth Sy.](#), *J. Advances in Modelling Earth*  
1274 *Systems*, 11, 752-770, 2019.
- 1275
- 1276 Zeng. Y., Janjic, T., Lozar, A. de, Blahak, U., Reich, H., Keil, C., and Seifert, A.: Representation of model error in convective-  
1277 scale data assimilation: Additive noise, relaxation methods and combinations, [J. Adv. Model. Earth Sy.](#), *J. Advances in*  
1278 *Modelling Earth Systems*, 10, 2889–2911, 2018.
- 1279
- 1280 Zeng, Y., Blahak, U., and Jerger, D.: An efficient modular volume-scanning radar forward operator for NWP models:  
1281 description and coupling to the COSMO model, [Q. J. Roy. Meteor. Soc.](#), *Quarterly Journal of the Royal Meteorological Society*,  
1282 142(701), 3234-3256, 2016
- 1283
- 1284 Zhu, K., Xue, M., Ouyang, K., and Jung, Y.: Assimilating polarimetric radar data with an ensemble Kalman filter: OSSEs with  
1285 a tornadic supercell storm simulated with a two-moment microphysics scheme, [Q. J. Roy. Meteor. Soc.](#), *Q.-J.-R. Meteorol. Soc.*,  
1286 146: 1880– 1900, [doi:10.1002/qj.3772](https://doi.org/10.1002/qj.3772), 2020.
- 1287
- 1288



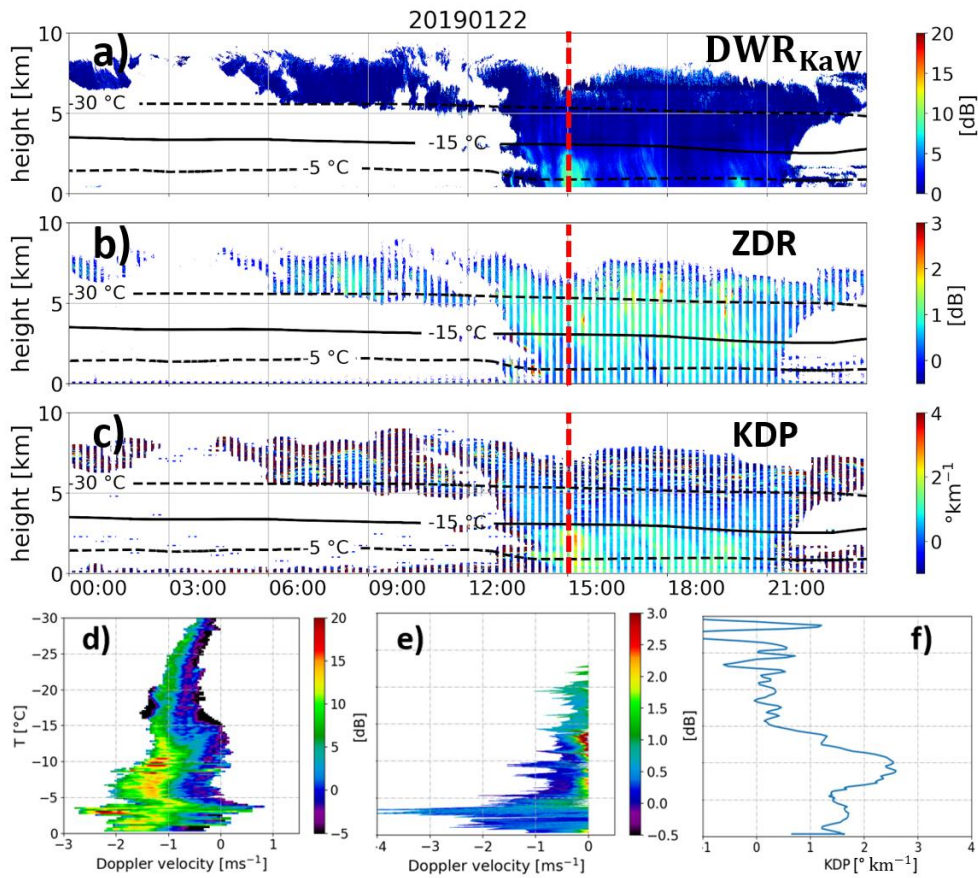


Figure 1: Observations at JOYCE-CF shows a) DWR<sub>KaW</sub>, b) Z<sub>DR</sub> (measured at a 30° elevation angle), c) K<sub>DP</sub> (also measured at 30° elevation angle) on 22 January 2019. Panels d)-f) show the observed DWR-spectrum, Z<sub>DR</sub>-spectrum and K<sub>DP</sub>-profile at 15:00 UTC (indicated by the red line in panels a)-c))

1289  
1290  
1291  
1292  
1293  
1294  
1295  
1296

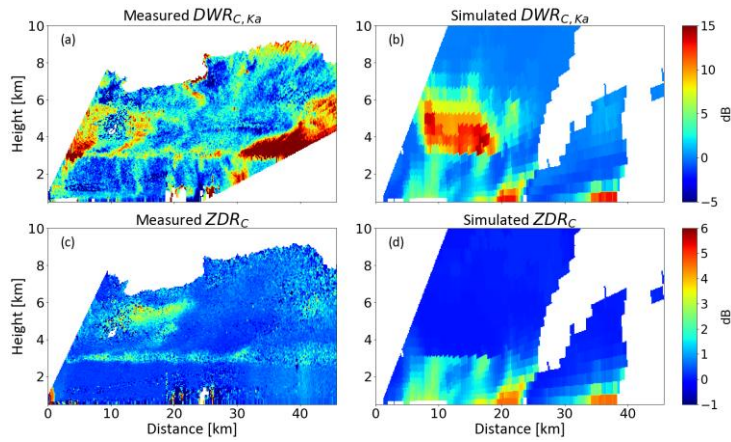


Figure 2 (a) Dual-wavelength ratio between the C-band POLDIRAD and Ka-band miraMACS measurements on the 7th July 2019, (b) simulated dual-wavelength ratio, (c) Differential radar reflectivity  $ZDR$  measured by the C-band radar POLDIRAD, (d) Simulated dual-wavelength ratio and (d) simulated  $ZDR$  of a comparable, but not identical, precipitation event using the P3 scheme (Morrison and Milbrandt, 2015).

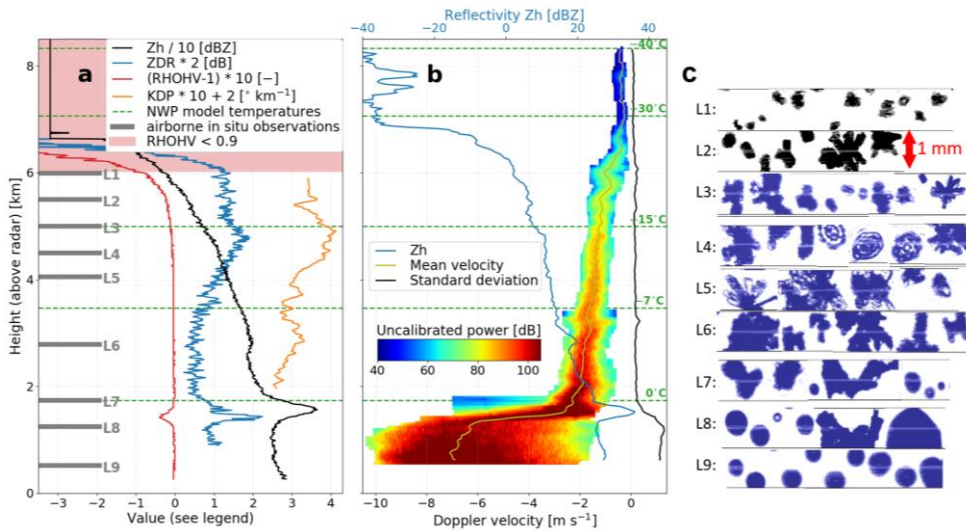


Figure 3: Measurements of slant-viewing and zenith-pointing polarimetric C-band weather radar scans with NWP model based temperature levels and airborne in-situ observations: (a) quasi-vertical profiles (QVPs) of radar reflectivity  $Z_H$ , differential reflectivity  $Z_{DR}$ , copolar cross-channel correlation coefficient  $\rho_{HV}$ , and the specific differential phase  $K_{DP}$  estimated from (noisy) measurements of the differential phase by aggressive filtering above the melting layer; (b) average Doppler spectra from a 15 s birdbath scan and corresponding first 3 moments at each radar bin height: reflectivity, power-weighted mean velocity and standard deviation; (c) in situ particle images (downward-looking projection images) collected at altitudes L1 to L9.

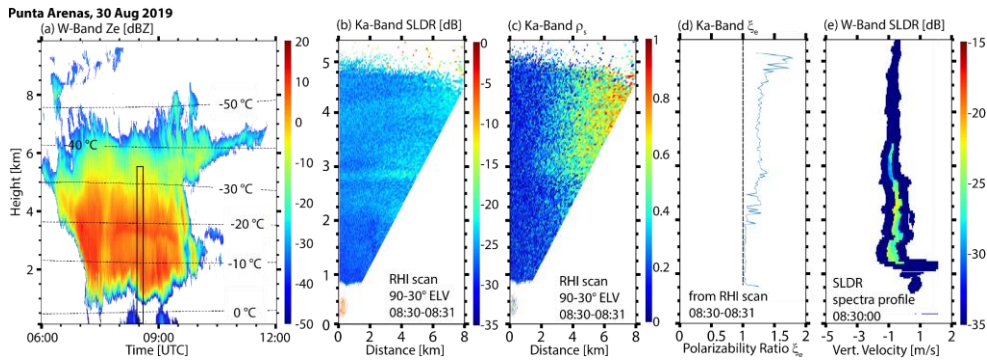
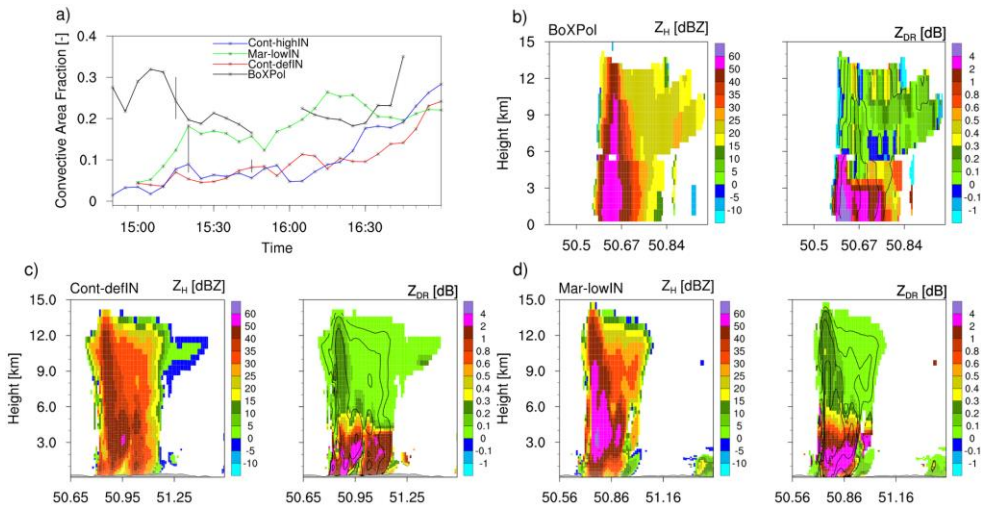
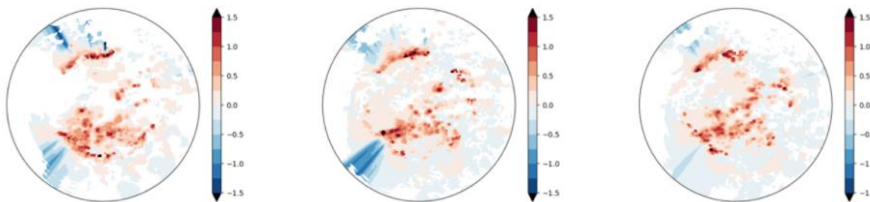


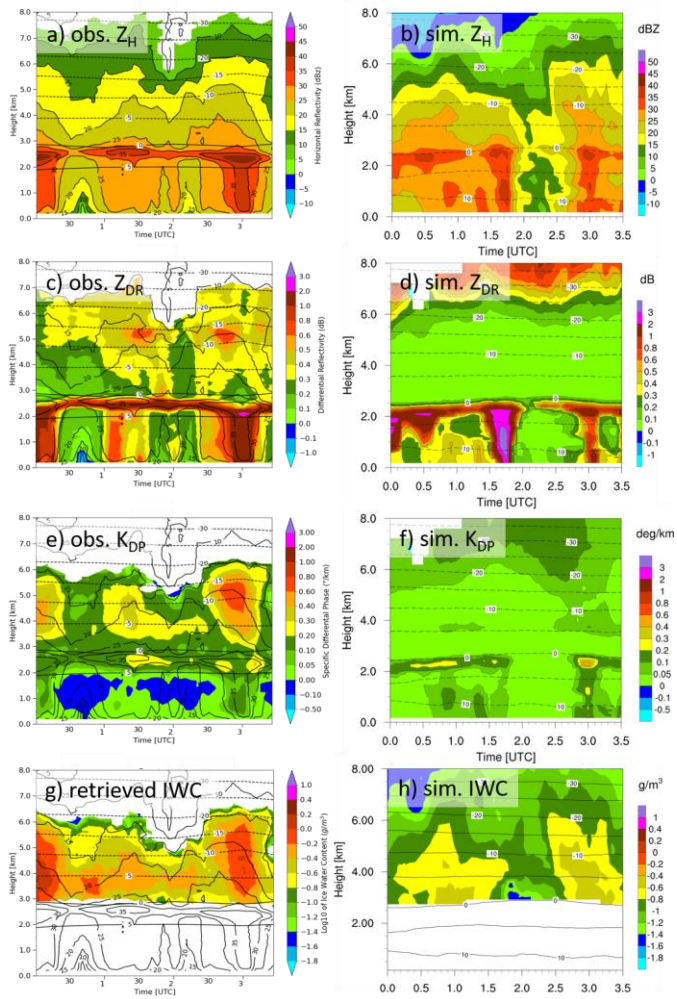
Figure 4: Case study of a deep mixed-phase cloud event observed with multiwavelength polarimetric cloud radars at Punta Arenas, Chile, on 30 August 2019. (a) vertical-pointing W-Band (94-GHz) radar reflectivity factor  $Z_e$  and isolines of modelled air temperature, (b) and (c) Ka-Band (35-GHz) RHI scans (90°-30° elevation) of slanted linear depolarization ratio SLDR and co-cross correlation coefficient in the slanted basis  $\rho_s$ , respectively, from 08:30-08:31 UTC, (d) profile of the shape index polarizability ratio ( $\xi_{sh}$ ) obtained from the RHI scans shown in (b) and (c), and (e) height spectrogram (at 90° elevation) of W-Band SLDR from 08:30:00 UTC. The time and height frame of panels (b-e) is indicated by the black rectangle in (a).



1320  
1321  
1322 **Figure 5: Time-series of Convective Area Fraction (CAF) evolution (panel a) and reconstructed observed (panel b) and**  
1323 **simulated/synthetic range-height-indicators (RHI) of horizontal reflectivity  $Z_H$  and differential reflectivity  $Z_{DR}$  (panels c and d).**  
1324 **Synthetic RHIs are based on simulations for actual land-cover with different perturbations of CN and IN concentrations, where**  
1325 **Cont-defIN indicates continental aerosol with default IN concentration and Mar-lowIN indicates maritime aerosol with low IN**  
1326 **concentration. The gaps in the BoXPol-observed CAF time series are due to strong attenuation. The vertical grey bars (panel a)**  
1327 **indicate the times at which the RHIs are compared.**  
1328



1329  
1330 **Figure 6: Synthetic PPI of  $Z_{DR}$  at 0.5 deg elevation for the DWD radar site Neuheilenbach based on the analysis obtained for June**  
1331 **4 at 16:00 UTC by assimilation of radar reflectivity and using three different ways to specify the model error: large scale uncertainty**  
1332 **(left), large plus unresolved scales uncertainty (middle) and in addition the use of the warm bubble approach (right).**



1333

1334

1335

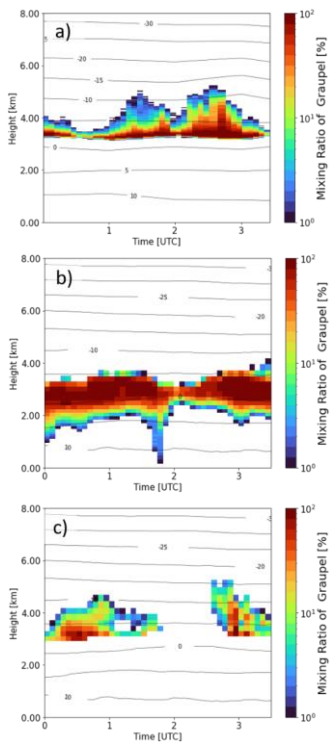
1336

Figure 7: Quasi-vertical profiles (QVPs) of observed (left column) and simulated (right column) polarimetric radar variables (right column), i.e. horizontal reflectivity  $Z_H$  (panels a and b), differential reflectivity  $Z_{DR}$  (panels c and d), specific differential phase  $K_{DP}$  (panels e and f), together with radar-retrieved ice water content (IWC<sub>r</sub>, panel g) and simulated ice water content (IWC<sub>s</sub>, panel h).



1337 The QVPs show a stratiform rain event observed on 7 October 2014 between 0:00 and 3:30 UTC with the polarimetric X-band radar  
1338 in Bonn, BoXPoL, and simulated with COSMO version 5.1 and the 2-moment cloud microphysics scheme.

1339



1340

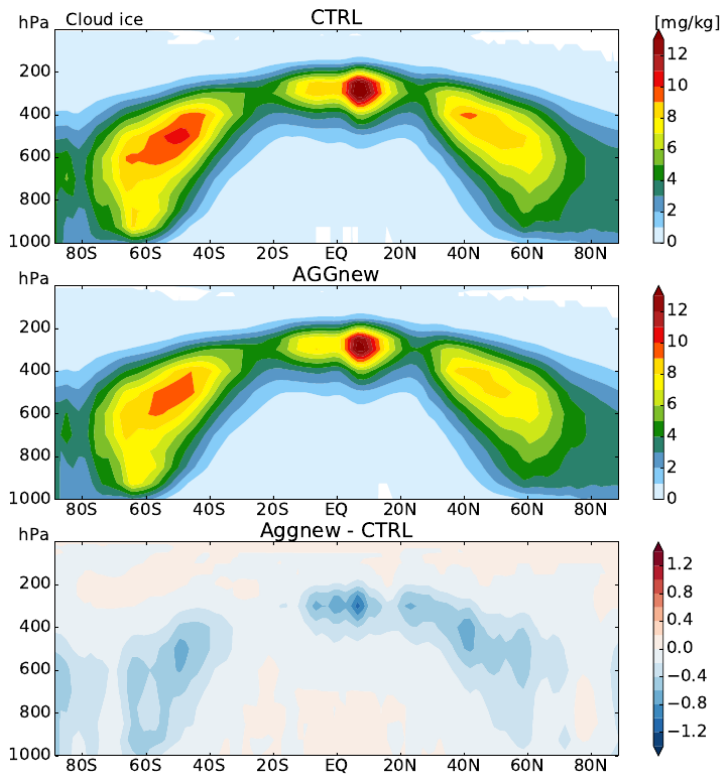
1341 **Figure 8: Retrieved and simulated graupel mixing ratios, defined as the percentage of graupel in the total hydrometeor mass, for**  
1342 **the stratiform rain event shown in Fig. 7 (7 October 2014, 0:00-3:30 UTC). An advanced hydrometeor classification and**  
1343 **quantification algorithm has been applied to polarimetric BoXPoL measurement (panel a) and to simulated radar variables based**  
1344 **on COSMO simulations (panel c) and compared to the COSMO-simulated graupel mixing (panel b).**

1345

1346

1347

1348



1349

1350 **Figure 9: Specific ice water,  $q_i$  [ $\text{g kg}^{-1}$ ] as zonal, annual mean for (top) standard ICON GCM output, (middle) aggregation**  
1351 **parameterization revised as stochastic parameterization drawing from the  $q_i$  subgrid-variability PDF, and (bottom) difference**  
1352 **between the two.**

1353

1354

1355

1356

1357

